Accepted Manuscript

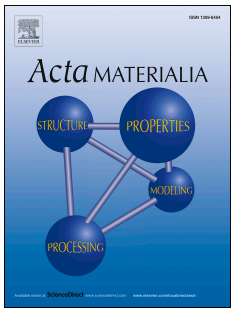

Nucleation and twinning in tin droplet solidification on single crystal intermetallic compounds

Z.L. Ma, J.W. Xian, S.A. Belyakov, C.M. Gourlay

PII: S1359-6454(18)30155-1

DOI: 10.1016/j.actamat.2018.02.047

Reference: AM 14402

To appear in: *Acta Materialia*

Received Date: 6 December 2017

Revised Date: 21 February 2018

Accepted Date: 22 February 2018

Please cite this article as: Z.L. Ma, J.W. Xian, S.A. Belyakov, C.M. Gourlay, Nucleation and twinning in tin droplet solidification on single crystal intermetallic compounds, *Acta Materialia* (2018), doi: 10.1016/j.actamat.2018.02.047.

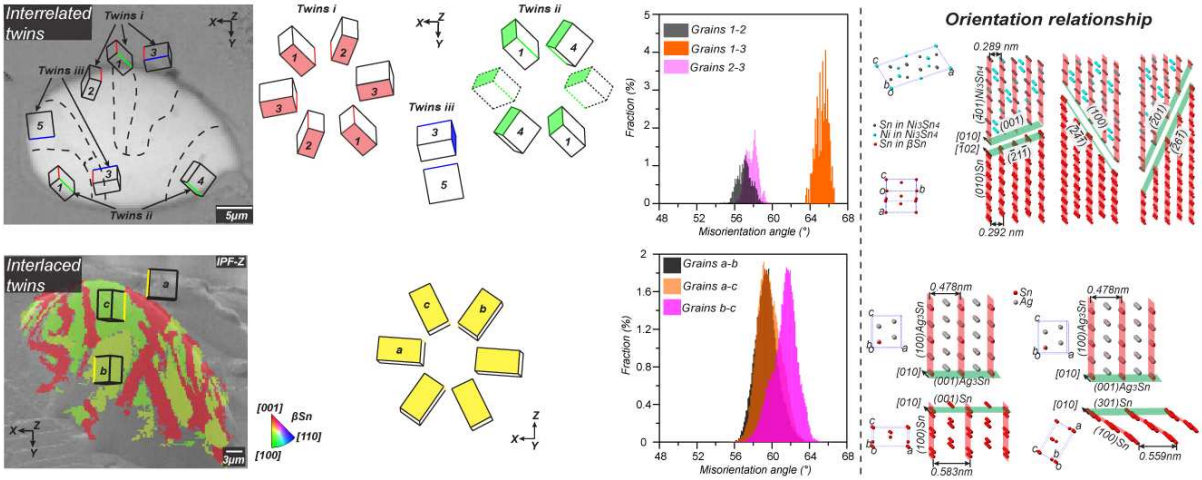

Nucleation and twinning in tin droplet solidification on single crystal intermetallic compounds

Z.L. Ma[1*], J.W. Xian[1], S.A. Belyakov[1], C.M. Gourlay[1]

[1] Department of Materials, Imperial College London, London. SW7 2AZ. UK

*z.ma13@imperial.ac.uk; +86 15801018340

Keywords: intermetallics; EBSD; orientation relationship; nucleation; twinning

Abstract

βSn nucleation is a key step in the formation of microstructure in electronic solder joints. Here, the heterogeneous nucleation of βSn is studied in undercooled tin droplets spread on the facets of various intermetallic compounds (IMCs). Nucleation undercoolings are measured in solidifying droplets and are linked to orientation relationships (ORs) measured by electron backscatter diffraction (EBSD). Preferred ORs developed on all IMCs studied. For the more potent nucleants (α$CoSn_3$, $IrSn_4$, $PtSn_4$, $PdSn_4$) the ORs represent relatively simple atomic matches. ORs with lower potency nucleants (Cu_6Sn_5, Ag_3Sn, Ni_3Sn_4) had more complex atomic matches that are explored based on matching of the closest packed atomic rows. βSn solidification twinning is shown to be more complex than has been reported previously: both nucleation on an IMC facet and cyclic twinning of that grain occurred in many droplets on Cu_6Sn_5, Ag_3Sn, Ni_3Sn_4; in all twinned droplets the $<100>_{Sn}$ twinning axis occurred along a direction on the IMC with the lowest linear atomic disregistry; and interrelated cyclic twins formed consisting of up to five rings of cyclic twins all related by shared $<100>_{Sn}$ axes.

1 INTRODUCTION

The solidification of electronic solder joints typically occurs from a single βSn nucleation event in a small volume of undercooled liquid. This commonly generates βSn cyclic twins involving {101} or {301} type twins with 57.2° and 62.8° rotations around <100> respectively [1]. In the case of Sn-Ag and Sn-Ag-Cu, solidification twinning creates beachball and interlaced βSn microstructures [1-5] whereas, in Sn-Cu and Sn-Cu-Ni, twinning usually creates βSn plate structures [1, 3, 6-9]. Similar twinning also occurs in Sn-Zn solders [10]. It has been shown that twinned solder joints perform differently in service than single-grain joints [11] and that interlaced twinned microstructures can improve creep performance [12] Since these twinned microstructures appear to be related with βSn nucleation and/or the early stages of growth, a deeper understanding of solidification twinning requires fundamental studies on the βSn nucleation process.

Catalysing βSn nucleation has been intensively studied in recent years [9, 10, 13-18] in order to prevent large and variable nucleation undercoolings [2, 4, 19, 20], excessive dissolution of Cu substrates [21, 22], and large primary intermetallic compounds (IMCs) such as Cu_6Sn_5 rods and Ag_3Sn plates in solder joints [23-27]. This body of work has identified a range of additions that reduce the βSn nucleation undercooling (e.g. Zn, Al, Ti, Mn, Co, Ir, Pd, Pt), and heterogeneous nucleants for βSn have been identified such as the family of transition metal stannides that includes $\alpha CoSn_3$, $PtSn_4$, $PdSn_4$, and $\beta IrSn_4$ which are a relatively good lattice match to βSn and can be used to control βSn nucleation and orientation(s) in joints [28].

Furthermore, various researchers have suggested that the common solder IMCs Cu_6Sn_5 [6, 29, 30], Ag_3Sn [24, 31], and Ni_3Sn_4 [32] can catalyse βSn nucleation, although there is limited information on the heterogeneous nucleation mechanisms in these cases. Since Cu_6Sn_5,

Ag_3Sn, and/or Ni_3Sn_4 form prior to βSn nucleation as primary phases and interfacial reaction layers in most joints, it is important to understand how they influence βSn nucleation and twinning.

In this paper, a recently developed experimental approach to studying heterogeneous nucleation [28] is used to gain insights into the nucleation and twinning of βSn in electronic soldering. The approach involves solidifying 5 – 100 μm droplets of Sn on the fluxed facets of IMC single crystals, measuring the nucleation undercooling by DSC and investigating ORs by EBSD without any mounting/grinding/polishing. The key advantages of this technique are that nucleation ORs can be measured directly by EBSD, and the relative simplicity allows hundreds of droplets to be studied and statistically significant datasets to be collected.

This work was conducted to (i) directly test whether βSn can nucleate heterogeneously on a range of intermetallic compounds including the common solder IMCs: Cu_6Sn_5, Ni_3Sn_4, and Ag_3Sn, (ii) compare nucleation on Cu_6Sn_5, Ni_3Sn_4, and Ag_3Sn with that on relatively potent IMC nucleants: $PdSn_4$, $PtSn_4$, $\beta IrSn_4$ and $\alpha CoSn_3$, (iii) explore whether preferred nucleation ORs exist between βSn and each of the IMCs, and (iv) gain deeper insights into the link between βSn nucleation and solidification twinning.

2 METHODS

$\alpha CoSn_3$, $PtSn_4$, $PdSn_4$, $\beta IrSn_4$, Cu_6Sn_5, Ag_3Sn and Ni_3Sn_4 were grown in Sn-rich binary alloy melts and were then extracted as single crystals by selective dissolution of the βSn after solidification. Hypereutectic Sn-X (X= 0.1Co, 0.2Pt, 0.5Pd, 1Ir, 1.1Cu, 0.5Ni, 4Ag all in wt%) alloys were used, prepared by holding the specified amounts of 99.9% purity tin and 99.9% X in evacuated quartz ampoules for 168 h at 1200 °C. Alloys were reheated to 400 °C and cooled at 0.004 K/s to grow the desired IMCs. Finally, to dissolve βSn and release the single crystal IMCs, a solution of 5% NaOH and 3.5% ortho-nitrophenol in distilled water was used.

To wet and spread liquid tin droplets on the facets of the IMCs, particles of 99.9% Sn powder with size ~5 – 100 µm were placed on the single crystal IMCs covered with a $ZnCl_2$-NH_4Cl based soldering flux (Stay-Clean®, HARRIS), and reflowed in a forced air convection reflow oven with thermal profile of heating rate 1 K/s, peak temperature 240 °C, liquid time ~80 s, and cooling rate ~3 K/s. Flux residues were cleaned off in ethanol in an ultrasonic bath and then samples were reflowed again in a Mettler Toledo DSC under a N_2 atmosphere. The heating rate was 0.17 K/s, the maximum temperature was 240 °C and the cooling rate was 0.33 K/s. To measure βSn nucleation undercoolings, a sample (a single Sn droplet of size ~40-75µm on an IMC facet) was cycled 5-20 times in the DSC. The βSn nucleation undercooling was defined as the eutectic melting onset on heating minus the solidification onset on cooling. Typical DSC heating and cooling curves for single ~40µm Sn droplets are shown in Supplementary Information Figure 1. 4-9 samples were measured separately for each IMC phase resulting in at least 50 undercooling values for each IMC. In separate experiments, numerous Sn droplets were solidified on IMC facets using the same DSC thermal profile to generate multiple droplets on IMC facets for EBSD studies.

Figure 1 overviews the droplet technique used here. Figure 1 (A) is a schematic Sn-X (X=Co, Pt, Pd, Ir, Cu, Ni) phase diagram at the Sn-rich corner; the phase at the right side is the IMC studied for each Sn-X system. Note that, in all cases, the IMCs studied are the most Sn-rich compounds in the binary Sn-X system. When a Sn droplet wets and spreads on a single crystal IMC at the peak temperature of 240 °C, the liquid must dissolve some of the IMC to increase the concentration of X in the liquid to the equilibrium value of C_L^{240}. During subsequent solidification, the possible mechanisms for βSn nucleation are summarised in Figure 1 (B) as: 1) homogeneous nucleation; 2) heterogeneous nucleation on the IMC, which can be 2a) heterogeneous nucleation on the flat facet or 2b) heterogeneous nucleation on growth ledges or other surface defects of the IMC [33, 34]; and/or 3) heterogeneous nucleation on other phases such as primary IMCs, impurity phases, or oxides.

To explore the active mechanisms and resulting growth microstructures, analytical scanning electron microscopy (SEM) was performed in a Zeiss AURIGA field-emission gun-SEM (Carl Zeiss, Oberkochen, Germany) equipped with an Oxford Instruments INCA x-sight energy dispersive x-ray (EDX) detector (Oxford Instruments, Oxfordshire, UK) and an e-Flash Bruker electron backscatter diffraction (EBSD) detector (Bruker AXS Inc., Fitchburg, WI). Each IMC has been identified by detailed XRD studies previously [35-42] and were confirmed here by combining EDX with EBSD. The crystal structures used for EBSD indexing are summarised in Table 1. Note that Cu_6Sn_5 has multiple polymorphs [43-46] which could all be fit to the EBSD patterns and that the high-temperature hexagonal ηCu_6Sn_5 [40] was used for EBSD indexing because it is the stable phase at the βSn nucleation temperatures. The microstructures and orientation relationships (ORs) between the βSn droplets and IMC facets were measured by EBSD directly on the IMCs and βSn droplets without further sample preparation.

To study the surface of the partially-dissolved IMC (Figure 1 (B)), some Sn droplets on IMCs were etched in 5% NaOH and 3.5% orthonitrophenol in H_2O to remove all βSn. The IMC surface was then studied by SEM imaging. 3D tomographs of some droplets were obtained by slice & view using a focused ion beam (FIB) of 2.8 nA and a slice distance of 200 nm in a FEI Helios Nanolab (FEI, Hillsboro, Oregon). Raw images were processed using ImageJ and Matlab, and then Avizo 7 was used for 3D reconstruction and analysis of the droplet and IMC.

3 RESULTS AND DISCUSSION

3.1 Nucleation of βSn on $PdSn_4$, $\alpha CoSn_3$, $PtSn_4$, and $\beta IrSn_4$

SE-SEM images of typical single crystals of $\alpha CoSn_3$, $PtSn_4$, $PdSn_4$, and $\beta IrSn_4$ are shown in Figure 2 (A). All have a similar morphology of near-square plates which has been described as tile-like previously [4, 28, 47]. The largest facet of these orthorhombic or tetragonal single crystal IMCs are identified as $(100)_{\alpha CoSn3}$, $(010)_{PtSn4}$, $(010)_{PdSn4}$, and $(001)_{\beta IrSn4}$, by EBSD as shown in Figure 2 (A) where the unit cell orientations have been plotted from the measured Euler angles. Note that these phases have been assigned different space groups by different authors and the indexing in this work refers to the crystallographic descriptions in Table 1.

A typical Sn droplet solidified on a facet is shown in Figure 2 (B) using $\alpha CoSn_3$ as an example. It can be seen that the liquid Sn wet and spread into a hemispherical cap before solidification. Figure 2 (C) shows 5 typical Sn droplets on a $PdSn_4$ (010) facet. Orientations of the βSn and $PdSn_4$ were measured by EBSD and are shown as wireframe unit cells in Figure 2 (C) and by the EBSD IPF-Y map in Figure 2 (D). All βSn grains contain a single orientation that can be classified into two types: the orientation shown by green unit cell wireframes and that shown by the orange wireframe. The $PdSn_4$ wireframe unit cell is plotted in black in Figure 2 (C). The two βSn orientations correspond to two ORs with $PdSn_4$ respectively:

$$(010)_{PdSn4}||(100)_{Sn} \text{ with } [100]_{PdSn4}||[001]_{Sn} \quad \text{Eq. 1}$$

$$(010)_{PdSn4}||(100)_{Sn} \text{ with } [001]_{PdSn4}||[001]_{Sn} \quad \text{Eq. 2}$$

These two ORs are plotted in pole figures in Figure 2 (E) and are indicated by the common circles, squares, and triangles of the same colour as the βSn unit cell wireframes in Figure 2 (C) and IPF-Y map in Figure 2 (D).

The βSn orientations of 117 droplets on $PdSn_4$ crystals are summarized into a stereographic projection in Figure 2 (F) with the IMC facet-normal at the centre. Each droplet solidified into a single βSn orientation and all measured βSn orientations have been rotated towards one representative orientation by exploiting symmetry. The mean ± standard deviation (measured from all EBSD points of different droplets/grains) of three pairs of parallel planes are given. In all cases, the βSn had one of the ORs with $PdSn_4$ in Eq. 1 and 2 with angular deviations <4°.

Similar investigations were performed on Sn droplets on $\alpha CoSn_3$, $PtSn_4$, and $\beta IrSn_4$ plates in reference [28]. The $PdSn_4$ data and the data from reference [28] are combined into a single dataset in Table 2 which summarises the EBSD-measured ORs and the statistics of occurrence of each OR. As shown in Table 2, all droplets had highly reproducible ORs on these IMCs.

The mean nucleation undercooling of ~40-75 µm Sn droplets on $\alpha CoSn_3$, $PtSn_4$, $PdSn_4$, and $\beta IrSn_4$ is shown by the 'grey' bars in Figure 3. There are at least 50 measurements for each case. Note that this data comes from droplets with a range of diameters of ~35 µm (~40-75 µm) which is likely to influence the nucleation undercooling values. However, the size distribution of the droplets in each case (freestanding or on IMCs) are the same since droplets are selected from the same powder. Therefore, the nucleation undercoolings of different cases are comparable. It is clear that droplets on these four IMCs show substantially suppressed nucleation undercooling when comparing with ~40-75 µm freestanding Sn droplets (labelled 'Sn ball'). Combining the suppressed undercooling and the reproducible OR(s), it can be inferred that βSn nucleated heterogeneously on the IMC facet in every droplet by mechanism 2a or 2b in Figure 1 (B). At the same time, it is striking in

Figure 3 that the undercoolings are large relative to most studies of potent heterogeneous nucleants. In large part, this is due to the small size of the Sn droplets since previous studies on large (60 g) samples measured nucleation undercoolings of less than 1 K for alloys containing $\alpha CoSn_3$, $\beta IrSn_4$, $PdSn_4$ or $PtSn_4$ [10]. This size effect can be seen further in Figure 3 where undercooling data are also shown for ~550 µm balls made from the 7 Sn-X hypereutectic alloys.

3.2 Nucleation of βSn on Cu_6Sn_5

A typical Cu_6Sn_5 single crystal is shown in Figure 4 (A) and (B). It has a hexagonal rod-like morphology. EBSD analysis showed that its main facets and the direction along the rod are $\{10\bar{1}0\}_{Cu6Sn5}$ and $[0001]_{Cu6Sn5}$ respectively as shown by the wireframe unit cell and Euler angles on Figure 4 (A) and labels on Figure 4 (B). This morphology is consistent with past work [48-51].

Figure 4 (C) shows 8 typical Sn droplets on a $(10\bar{1}0)_{Cu6Sn5}$ facet with unit cell wireframes superimposed. As shown in Figure 4 (C) and the EBSD IPF-X map in Figure 4 (D), these βSn droplets are either single-grain (droplets 2 and 6) or contain multiple grains (droplets 1, 3, 4, 5, 7 and 8).

EBSD revealed that all multiple-grain Sn droplets contain all or some βSn grains that are solidification twins (i.e. ~60° rotations about a shared <100> as discussed in [1]) as indicated by the same coloured <100> axes on the βSn unit cells in Figure 4 (C). Some of the multiple-grain Sn droplets (droplets 3, 4, 5 and 8) have βSn grains that are all interrelated with each other by twinning (e.g. droplet 3), while others do not (e.g. droplet 1 contains two grains related by twinning and a third independent grain).

Droplet 3 is shown in more detail in Figure 5 as a typical example of multiple interrelated cyclic twins. This Sn droplet contains grains that are twinned about three different <100> axes, indicated by red-twins i, green-twins ii, and blue-twins iii. Cyclic twins i and ii share a common grain '1' and cyclic twins i and iii share a common grain '3', as shown in Figure 5 (A). This can also be seen in the <100> pole figure of βSn in Figure 5 (B), in which <100> poles of different grains are numbered and dashed lines indicate the trace of the common {100}.

Note that the common axes (dashed circles) of cyclic twins ii and iii are in the common plane of cyclic twins i (Figure 5 (B)). These interrelated twins are further shown in Figure 5 (C) by plotting the unit cells of the 5 orientations from the measured Euler angles and translating the unit cells to make clear the cyclic twinning. The common {100} and <100> of each cyclic twins are shaded red, green and blue for cyclic twins i, ii and iii respectively. The dashed unit cell in green-twins ii was not measured experimentally but is shown for clarity. Each cyclic twin is shown twice, first arranged as {101} cyclic twins and then translated into {301} cyclic twins to depict the different spatial relationships.

Figure 5 (D) quantifies the angular deviation between the <100> twinning axes (δ_{ij}), the misorientation between the other <100> (ω_{ij}), and the in-grain misorientation (m_i) for each of grains 1, 2, and 3 in twins i (Figure 5 (A)). δ and ω are defined schematically in Figure 5 (C). The angles in Figure 5 (D) are the mean $\pm$ the standard deviation using the Euler angles from all points in grains 1, 2, and 3 in the EBSD map. For a perfect twin, $\delta_{ij} = 0$, $m_{ii} = 0$, and $\omega_{ij} = 57.2°$ for {101} twins and 62.8° for {301} twins. For grains 1, 2, and 3, δ_{ij} and m_{ii} are < 3° in all cases and the standard deviations in ω_{ij} are ≤ 1° (Figure 5 (D)). These values are significantly smaller than in BGA-scale balls/joints [1, 4, 8], where typical values are $\delta_{ij} = 4°$, $m_{ii} = 6°$, and the typical standard deviation in ω_{ij} is 6° [4]. This is an advantage of the technique used here where (i) the small droplet size gives little growth distance in which angular deviations can develop and (ii) the absence of grinding/polishing prevents βSn deformation. By comparing the values of ω_{ij} in Figure 5 (D) and the histograms of misorientation angle in Figure 5 (E), it can be seen that the misorientation distribution between grains 1, 2, and 3 can be distinctly separated with two peaks consistent with {101} twinning (57.2°) and one peak close to {301} twinning (62.8°) [1]. Examination of multiple

droplets on Cu_6Sn_5 showed a similar result: two grain pairs are misorientated close to one twinning angle and the other is misoriented close to the other twinning angle. Despite this, for simplicity, in Figure 5 and subsequent Figures cyclic twinning is plotted as all {101} twinning and/or all {301} twinning.

Some βSn grains (labelled with red unit cell wireframes in droplets in Figure 4 (C)) had a preferred OR with Cu_6Sn_5. Typical examples are shown for droplets 4 and 6 in Figure 4 (C) whose pole figures and that of Cu_6Sn_5 are shown in Figure 4 (E). The OR is indicated by common circles, triangles, diamonds, and squares in the βSn and Cu_6Sn_5 pole figures. There are multiple near-parallel pairs of planes for both droplets 4 and 6 and, in both cases, the OR with Cu_6Sn_5 can be written as Eq. 3:

$$(10\bar{1}0)_{Cu6Sn5}||(111)_{Sn} \text{ and } [0001]_{Cu6Sn5}||[11\bar{2}]_{Sn} \qquad \text{Eq. 3}$$

Among 60 EBSD measured Sn droplets, 37 featured βSn grains with the above measured OR (Table 2 and 3) and the orientations of these grains with respect to Cu_6Sn_5 are summarised into the stereographic projection of 10 near-parallel planes and 16 near-parallel directions in Figure 4 (F) and (G). The mean misorientation for each pair of near-parallel planes is <~3°.

Note by comparing the pole figures of Cu_6Sn_5 in Figure 4 (E), that βSn grains in droplet 6 and droplet 4 have a different plane parallel with the Cu_6Sn_5 facet (indicated by the triangles in Figure 4 (E)); one is $\{241\}_{Sn}$, the other is $\{111\}_{Sn}$. These planes are indicated by bold font in Figure 4 (F). Table 2 shows that 5 out of 37 Sn droplets had $\{111\}_{Sn}$ parallel with the $\{10\bar{1}0\}_{Cu6Sn5}$ facet and the remaining 32 had $\{241\}_{Sn}$. The atomic matching associated with this OR and interface planes are discussed in our previous paper [6] and, therefore, are not discussed further here.

Table 3 summarises the βSn microstructures and ORs in all 60 droplets on Cu_6Sn_5. It can be inferred that there was one βSn nucleation event in each single-grain and twinned droplet (45 out of 60 droplets), and multiple βSn nucleation events in each droplet with multiple independent grains (15 out of 60). The presence or absence of an OR with Cu_6Sn_5 provides insights into the nucleation mechanisms: βSn most likely nucleated heterogeneously only on Cu_6Sn_5 in the 28/60 single-grain and twinned droplets with the OR in Eq. 3 by mechanism 2a or 2b in Figure 1 (B); in the 9/60 multiple-independent-grain droplets with the OR in Eq. 3 βSn nucleated by both mechanisms 2a/2b and 3 in Figure 1 (B); and the remaining 23/60 droplets with no reproducible OR most likely nucleated on other phases (or geometrically catalytic sites such as grooves and ridges in the oxide layer) that are more potent than Cu_6Sn_5 by mechanism 3 in Figure 1 (B).

The different nucleation mechanisms in droplets on Cu_6Sn_5 indicate that there was competition among nucleation sites (i.e. between mechanism 2 and 3 in Figure 1 (B)). Examining the nucleation undercooling for βSn on Cu_6Sn_5 in Figure 3, it can be seen that the mean undercooling on Cu_6Sn_5 (53 K) is only slightly less than with no IMC substrate (58 K) and that there is overlap over a wide range of undercooling values. From this, it can be seen that the $\{10\bar{1}0\}$ facet of Cu_6Sn_5 is only weakly catalytic to βSn nucleation and, in some droplets, other sites that are naturally present in the droplet were more potent than Cu_6Sn_5.

3.3 Nucleation of βSn on Ni_3Sn_4

A typical Ni_3Sn_4 single crystal is shown in Figure 6 (A) and (B). EBSD measurements showed that there are three main facets: $(100)_{Ni3Sn4}$, $(\bar{2}01)_{Ni3Sn4}$, and $(001)_{Ni3Sn4}$ and the direction along the rod is $[010]_{Ni3Sn4}$. These are consistent with ref. [52].

Typical examples of Sn droplets on a (100) facet of Ni_3Sn_4 are shown in Figure 6 (C) and the measured EBSD IPF-X map of these droplets is shown in Figure 6 (D). Similar to the Sn droplets on Cu_6Sn_5, single-grain (e.g. droplets 1, 5, and 6), simple-twins (droplets 2 and 3), interrelated-twins (e.g. droplets 4 and 7), and multiple-independent-grain microstructures were all found in droplets on the different facets of Ni_3Sn_4. Unit cell wireframes are superimposed in Figure 6 (C) to show grain orientations, and green, pink, and yellow are used to indicate the twinning axes. The interrelated twins had similar features to those shown in Figure 5 for droplets on Cu_6Sn_5. Twinning angles could be clearly separated with one/two close to {101} twinning and the other(s) close to {301} twinning.

Some βSn grains in droplets on the different facets of Ni_3Sn_4 had reproducible ORs with the Ni_3Sn_4. In Figure 6 (C), those grains with the OR are indicated by red unit cell wireframes. The OR between a typical red-wireframe βSn grain (droplet 1) and the {100} facet of Ni_3Sn_4 is shown in the pole figures in Figure 6 (E) where near-parallel planes are indicated by common circles, triangles, and squares. The βSn plane parallel to the $\{100\}_{Ni3Sn4}$ facet is {241}, as shown by the superimposed triangles. This OR can be written as Eq. 4:

$$(100)_{Ni3Sn4}||(\bar{2}\bar{4}\bar{1})_{Sn} \text{ and } [0\bar{1}0]_{Ni3Sn4}||[10\bar{2}]_{Sn} \qquad \text{Eq. 4}$$

The same OR was measured in Sn droplets on $\{\bar{2}01\}_{Ni3Sn4}$ and $\{001\}_{Ni3Sn4}$ facets, indicating that the OR is independent of the facet plane of Ni_3Sn_4. βSn grains showing the above OR

were found in 112 out of 179 droplets (Table 2), and their orientations are summarised into a pole figure with respect to Ni_3Sn_4 in Figure 6 (F). 12 pairs of near-parallel planes are plotted, and the scalar misorientation angle between the planes (mean $\pm$ standard deviation from all EBSD points) is shown for each. The three Ni_3Sn_4 facets and their parallel planes in βSn are indicated by bold font. Figure 6 (G) is a similar stereographic projection plotting 8 pairs of near-parallel directions.

Figure 7 (A) is a plot of the OR in Eq. 4 and the interfaces on the three facets. The red shaded planes are the closest packed $\{100\}_{Sn}$ (Table 4) which is parallel with $\{\bar{4}01\}_{Ni3Sn4}$ and the d-spacing mismatch of them is ~1%. The three facets share a common parallel direction, $<010>_{Ni3Sn4}||<102>_{Sn}$. The planar atomic matches of the interfaces on the three facets are shown in Figure 7 (B). Red atoms represent Sn in βSn, gray atoms are Sn in Ni_3Sn_4, and transparent atoms have been projected into the plane. It can be seen that there is reasonable matching on some sites but the planar matches are not excellent and all the interface planes have at least one phase with zig-zag character as indicated by transparent atoms. The percentage occurrence of the OR (Eq. 4) on each facet is shown on Figure 7 (B), which is calculated from Table 2. Based on this, it might be expected that the βSn-Ni_3Sn_4 interfacial energy on these facets for this OR follows the order (001)>($\bar{2}$01)>(100).

At the same time, note that the nucleation plane does not need to be the macroscopic facet plane and could be another surface plane created by ledges etc. on the facet surface, as shown schematically in Figure 1 (B). To explore the lattice match further, we consider Zhang and Kelly's Edge-to-Edge theory [53, 54] which predicts that the lowest energy heterointerface should involve the closest or nearly closest packed planes in the two crystals meeting edge-to-edge at the interface with a good atomic match and that these planes

need not be parallel. With this configuration, some of the closest or nearly closest packed atomic rows (i.e. directions) should be parallel and arranged so as to minimise the linear disregistry along these rows. Table 4 shows a rank ordered list of (i) the planar atomic density and (ii) the interatomic distances along atomic rows in βSn and Ni_3Sn_4. Note that many planes and directions have zig-zag character in these phases and, therefore, densities and spacings have been calculated by projecting atoms into the planes or rows. Comparing Table 4 and Figure 6 (F) and (G) it can be seen that the two closest packed rows in βSn $[0\bar{1}0]$, [100] are parallel with the 2nd and 3rd closest packed rows in Ni_3Sn_4 $[10\bar{1}]$, $[\bar{1}\bar{5}\bar{4}]$ and, in each case, the linear disregistry is ~1%. These pairs of directions lie in the planes $(1\bar{1}1)_{Ni3Sn4}$ || $(00\bar{1})_{Sn}$. Similarly, $[0\bar{1}0]_{Ni3Sn4}$ || $[10\bar{2}]_{Sn}$ (5th II 4th with 6% linear disregistry) and $[10\bar{1}]_{Ni3Sn4}$ || $[0\bar{1}0]_{Sn}$ (2nd || 1st with ~1% disregistry) and lie in the planes $(101)_{Ni3Sn4}$ || $(\bar{2}0\bar{1})_{Sn}$. However, these planes are complex zig-zag planes so the planar lattice match is not as good as it appears from an analysis of rows. From this analysis of parallel rows and planes, it can be seen that the Edge-to-Edge theory [53, 54] is in reasonable agreement with our measured OR although the optimum interface plane is unclear.

Figure 3 shows that the nucleation undercooling for βSn in droplets on Ni_3Sn_4 is significantly smaller than on Cu_6Sn_5 and Ag_3Sn, indicating that Ni_3Sn_4 is more catalytic. This is consistent with the atomic matches of Sn/Cu_6Sn_5 as shown in ref. [6] and in Figure 7 (B), i.e. the atomic matches on the (100) and $(\bar{2}01)$ Ni_3Sn_4 facets are significantly better than those of $(1\bar{1}00)_{Cu6Sn5}||(\bar{2}41)_{Sn}$ and $(10\bar{1}0)_{Cu6Sn5}||(111)_{Sn}$, where the planar densities are quite different for βSn and Cu_6Sn_5 as shown in Ref. [6]. At the same time, the relatively high undercooling in droplets on Ni_3Sn_4 (compared with the $\alpha CoSn_3$, $PtSn_4$, $PdSn_4$, and $\beta IrSn_4$) is

likely to be due to the lack of a simple match in an interfacial plane (Figure 7 (B)) and their zig-zag features.

Table 3 and 2 summarise the βSn microstructures and ORs in all 179 droplets on Ni_3Sn_4. It can be inferred that there was a single βSn nucleation event in the single-grain and twinned droplets (159 out of 179) on the three facets of Ni_3Sn_4, and multiple βSn nucleation events in the droplets with multiple independent grains (20 out of 179). 104 out of 179 single-grain and twinned droplets had the OR in Eq. 4 which indicates that βSn nucleated heterogeneously only on Ni_3Sn_4 in these droplets by mechanism 2a or 2b in Figure 1 (B). 8/179 multiple-independent-grains droplets had both a grain with the OR (Eq. 4) and independent grains, showing that nucleation occurred on both the Ni_3Sn_4 and on other phases/sites in the same droplet (i.e. by both mechanisms 2 and 3 in Figure 1 (B)). In the remaining 67/179 droplets with no reproducible OR, it is likely that βSn nucleation happened on other phases/sites by mechanism 3 in Figure 1 (B). Thus, while Ni_3Sn_4 is more catalytic to βSn nucleation than Cu_6Sn_5 (Figure 3), there was competition between nucleation sites on Ni_3Sn_4 and Ni_3Sn_4 did not always act as a heterogeneous nucleant in the small droplets of this study. Table 2 highlights a stark contrast between Ni_3Sn_4 and $PtSn_4$, where the latter caused only a slightly smaller nucleation undercooling but always acted as a heterogeneous nucleant.

3.4 Nucleation of βSn on Ag_3Sn

A typical Ag_3Sn single crystal is shown in Figure 8 (A) and (B). It has a thin plate morphology and EBSD analysis identified the main facet to be $(001)_{Ag3Sn}$ and the edge directions to be $[100]_{Ag3Sn}$ and $[010]_{Ag3Sn}$. The measurements here are consistent with ref.[52, 55].

Figure 8 (C) shows 13 typical Sn droplets on a $(001)_{Ag3Sn}$ facet, and βSn orientations in these droplets are shown in the IPF-Z map in Figure 8 (D). Unit cell wireframes are superimposed to show the grain orientations, and green and yellow axes indicate different <100> twinning axes. Single-grain (e.g. droplets 9 and 11), simple-twins (e.g. droplet 13), interlaced-twins (e.g. droplets 1-8), interrelated-twins (e.g. droplet 10), and multiple-independent-grains (e.g. droplet 12) all formed in Sn droplets on Ag_3Sn. Interrelated twins in droplets on Ag_3Sn are similar to those in droplets on Cu_6Sn_5 (Figure 5) and Ni_3Sn_4. Interlaced twins (droplets 1 to 8 in Figure 8 (C)) were relatively common in droplets on Ag_3Sn. A typical example is shown in Figure 9 (A), in which the βSn grains exhibit an interlaced grain structure rather than distinct separate twin grains. In Figure 9 (D), the measured in-grain misorienation (m_i) and the deviation angles between the twinning axis (δ_{ij}) in these typical interlaced twins are slightly larger than the corresponding ones in twin i in the droplet on Cu_6Sn_5 shown in Figure 5 (D). The rotation angles ω_{ij} also have relatively large standard deviations, and the misorientation angles in Figure 9 (E) show substantially overlapping distributions with mean values close to 60°. Therefore, we cannot clarify whether they are {101}/{301} twinning [1]. This uncertainty occurred in most twinned droplets on Ag_3Sn and is significantly different to twinned droplets on Cu_6Sn_5 and Ni_3Sn_4 which were typically similar to Figure 5 (E).

EBSD measurements indicate that some βSn grains had a reproducible OR with the Ag_3Sn. Examples of such grains are denoted by red wireframes in Figure 8 (C). Pole figures of the 'red' βSn grain in droplet 8 and Ag_3Sn are shown in Figure 8 (E). This OR is:

$$(001)_{Ag3Sn}||(001)_{Sn} \text{ and } [010]_{Ag3Sn}||[010]_{Sn} \quad \text{Eq. 5.}$$

The red-wireframe grains were commonly related with another one or two grains by ~60° twins (e.g. grains with blue wireframes in Figure 8 (C)), where the $<010>_{Sn}$ twinning axis was always parallel with $[010]_{Ag3Sn}$. Therefore, these blue-wireframe grains also have a reproducible OR with the Ag_3Sn as shown by the '8 All βSn' pole figures in Figure 8 (E). The OR between the twinned βSn grains and Ag_3Sn is:

$$(001)_{Ag3Sn}||(301)_{Sn} \text{ and } [010]_{Ag3Sn}||[010]_{Sn} \quad \text{Eq. 6.}$$

To clarify these ORs, Figure 9 (C) exhibits the relative orientations of the three βSn grains and the Ag_3Sn crystal by plotting the unit cell orientations from the Euler angles and applying the same 90° rotation along X to all to aid visualisation (compare the coordinate systems in Figure 9 (A) and (C)). As shown in Figure 9 (C), βSn grains are cyclic twinned (the {101} type twinning arrangement is plotted here) and red-wireframe grains and blue-wireframe grains have {001} and {301} respectively parallel with the $\{001\}_{Ag3Sn}$ as indicated by the common black shaded planes in Figure 9 (C).

While the ORs in Eq. 5 and Eq. 6 were measured almost exactly in some droplets, many droplets had substantial rotations away from these ORs. The orientations of βSn grains from 145 out of 188 droplets are summarised into stereographic projections in Figure 8 (F) with respect to Ag_3Sn. The pole figures with red datapoints and blue datapoints indicate βSn orientations that have the same or similar ORs as Eq. 5 and Eq. 6 respectively. It can be seen

that, in both cases, the common $\{010\}_{Ag3Sn}||\{010\}_{Sn}$ (in both Eq. 5 and Eq. 6) has a relatively small mean misorientation angle of ~4°, while the other two pairs of planes exhibit much larger misorientation angles (>~10°). This large angular misorientation was found to be specific to Ag_3Sn and all other IMCs studied in this work had all near-parallel planes reproducibly within ~4° (e.g. Figure 2 (F), Figure 4 (F), and Figure 6 (F)).

The fixed common direction $[010]_{Ag3Sn}||[010]_{Sn}$ but variable common plane can possibly be understood by examination of the βSn-Ag_3Sn atomic lattice match in Figure 10. In Figure 10 (A) and (C), which represent ORs in Eq. 5 and Eq. 6 respectively, the closest packed $\{100\}_{Ag3Sn}$ meets with the closest packed $\{100\}_{Sn}$ either parallel on an $\{001\}_{Ag3Sn}||\{001\}_{Sn}$ interface or obliquely on an $\{001\}_{Ag3Sn}||\{301\}_{Sn}$ interface and there are large d-spacing mismatches (>14%) in both cases. However, there is a good atomic match (~2.7%) along $<010>_{Ag3Sn}||<010>_{Sn}$ which are the closest packed rows in each crystal (Table 4). Since there is good atomic match along only one direction, it is likely that the lowest energy interface is achieved by aligning the well-matched common direction, and the lack of other well-matched rows means that there is no strong preference for the common plane. This is in contrast to the other six IMCs in this study where there are multiple reasonably-well matched directions and a fixed OR.

The good matching along $[010]_{Ag3Sn}||[010]_{Sn}$ is probably also the origin of the $<100>_{Sn}$ twinning axis always being parallel to $[010]_{Ag3Sn}$, since this allows the good row matching between βSn and Ag_3Sn to be maintained in the twinned grains (Figure 9 (C)). The best matching direction(s) was also the twinning axis in twinned droplets on Ni_3Sn_4 and Cu_6Sn_5; on Ni_3Sn_4 (Figure 6 (G)), the twinning axis was either $[100]_{Sn}||[\ \bar{1}\bar{5}\bar{4}\ ]_{Ni3Sn4}$ or $[0\bar{1}0]_{Sn}||[10\bar{1}]_{Ni3Sn4}$ and both exhibit the lowest atomic mismatch in the Ni_3Sn_4-βSn OR of

0.7%; on Cu_6Sn_5 (Figure 4 (G)), the two <100> of βSn are parallel to two symmetrically equivalent <$10\bar{1}1$> in Cu_6Sn_5 and have the same lowest atomic mismatch in the Cu_6Sn_5-βSn OR of 1.4%.

All microstructures in droplets on Ag_3Sn are summarised in Table 3 along with their frequency of occurrence. Similar to Cu_6Sn_5 and Ni_3Sn_4, the microstructure types indicate the βSn nucleation mechanisms are: i) heterogeneous nucleation on Ag_3Sn by mechanism 2 in Figure 1 (B) in single-grain and twinned droplets (97 out of 188) that have the ORs in Eq. 5 and/or Eq. 6; ii) heterogeneous nucleation on other phases by mechanism 3 in Figure 1 (B) in droplets that show 'other' ORs with Ag_3Sn (43 out of 188); and iii) a mixture of heterogeneous nucleation on Ag_3Sn and heterogeneous nucleation on other phases in multiple-independent-grain droplets (48/188) that have a grain with the ORs in Eq. 5 and/or Eq. 6.

In Figure 3, it can be seen that the nucleation undercooling of single Sn droplets on Ag_3Sn is high compared with α$CoSn_3$, $PtSn_4$, $PdSn_4$, β$IrSn_4$, and Ni_3Sn_4, and only slightly more catalytic than no IMC facet (i.e. freestanding Sn droplets). This shows that Ag_3Sn is a low potency nucleant for βSn which is consistent with the relatively poor lattice match in Figure 10 with good matching along only a single direction. This is also consistent with better atomic matches on Ni_3Sn_4 facets (Figure 7 (B)).

3.5 IMC surface reconstruction

Figure 11 (A)-(G) shows typical surfaces of the IMCs after dissolving all βSn. The prior location of the droplets is visible for each IMC and each surface is partially-dissolved and/or reconstructed to some extent. It is clear that the dissolved IMC is much thicker (deeper) for $PdSn_4$ (Figure 11 (B)), Cu_6Sn_5 (Figure 11 (E)), and Ag_3Sn (Figure 11 (G)) compared with those of Ni_3Sn_4, α$CoSn_3$, $PtSn_4$, and β$IrSn_4$, in agreement with the calculated dissolved thickness Δh shown in Table 5 (details of the calculations can be found in the Supplementary Information). It can also be seen that primary $PdSn_4$ plates exist on the $PdSn_4$ facet (Figure 11 (B)), and no primary IMC was observed on the facets of other IMCs. Their absence in α$CoSn_3$, $PtSn_4$, β$IrSn_4$, and Ni_3Sn_4 is mainly due to their low volume fractions (f_{IMC}^{pri}) as indicated in Table 5. Relatively large volume fractions of primary IMCs are predicted in droplets on Cu_6Sn_5 and Ag_3Sn (Table 5) but are not present in Figure 11 (E) and (G). To test further for primary IMCs in Cu_6Sn_5 and Ag_3Sn, some of their droplets were studied by FIB-tomography. A 3D reconstructed droplet on Ag_3Sn is shown in Figure 11 (H)-(K). Figure 11 (K) shows that there are numerous eutectic Ag_3Sn particles (<~1μm) in the bulk but no primary Ag_3Sn. Therefore, the predicted primary Ag_3Sn is likely to have deposited on the Ag_3Sn facet during cooling from the peak temperature. This interpretation is corroborated by the average thickness of the final dissolved Ag_3Sn of ~0.05μm (Figure 11 (K)), which is close to the calculated result (0.04μm) assuming that all primary Ag_3Sn is deposited on the main Ag_3Sn plate during cooling from the peak temperature (see the Supplementary Information for further detail on this calculation).

Primary IMCs were only found in $PdSn_4$/Sn droplets and thus, on $PdSn_4$, there will have been competition between nucleation on the main $PdSn_4$ plate and the primary $PdSn_4$. However,

in Figure 11 (B), it can be seen that the primary $PdSn_4$ has the same orientation as the main plate and, therefore, nucleation competition will not affect the OR.

The micrographs in Figure 11 (A)-(G) and the FIB-tomography in Figure 11 (I)-(K) show that many IMCs have grooves and ledges on the main facet after partial dissolution and surface reconstruction. Thus, the interfacial plane at the nucleation site need not be the macroscopic facet plane and nucleation could have occurred by mechanism 2b in Figure 1 (B) in at least some of the droplets, particularly for lower potency Cu_6Sn_5, Ag_3Sn, and Ni_3Sn_4 where the extra catalysis from the grooves and ledges [6, 33, 34] may be important. It is also likely that surface grooves, ledges etc. affected the undercooling measurements in Figure 3 so that the undercooling is not a simple reflection of the lattice match but also a function of the geometrically catalytic features on the facet.

3.6 Insights into βSn nucleation and twinning in solder joints

The βSn microstructure in Sn droplets on $\alpha CoSn_3$, $PtSn_4$, $PdSn_4$ and $\beta IrSn_4$ was always a single grain without twinning (Table 3, Figure 2, and ref.[28]). Our previous studies on 550µm Sn-0.07Pt balls (containing $PtSn_4$) also measured single-grain or multiple independent-grain structures at both low and high cooling rate, with no solidification twinning [10]. However, Pd- [10] and Co- [4] microalloyed Sn-3.0Ag-0.5Cu-X balls/joints containing $PdSn_4$ and $\alpha CoSn_3$ particles often have cyclic-twinned (beach-ball like) microstructures, and cyclic-twinning has also been demonstrated in βSn that nucleates on the $\alpha CoSn_3$ layer when Sn-3Ag-0.5Cu is soldered on cobalt substrates [5]. This indicates that cyclic twinning of βSn that nucleates on $\alpha CoSn_3$ and $PdSn_4$ [4, 5, 10] depends on the presence of Ag and/or Cu solute. To test this, ~5-100 µm droplets of Sn-3Ag-0.5Cu were solidified on the (100) facet of $\alpha CoSn_3$ crystals. Typical results are shown in Figure 12 (A) where the droplet consists of three cyclically-twinned βSn orientations and one of the twinned grains (marked with an asterisk) has the OR in Table 2 with the $\alpha CoSn_3$. Combining this result with the 299/299 Sn droplets with no twinning on $\alpha CoSn_3$, $PtSn_4$, $PdSn_4$ and $\beta IrSn_4$ (Table 3), indicates that βSn nucleated heterogeneously on the $\alpha CoSn_3$ facet and the Ag and/or Cu solute promoted the development of cyclic-twins. However, solute may not be the only factor inducing solidification twinning, sample size (which affects the nucleation undercooling) and the concentration of Ag and/or Cu solute (which influences the solidification path) may also play important roles. For example, in ref.[28], where SAC305 solidified on Cu pads with added $\alpha CoSn_3$, $PtSn_4$, and $\beta IrSn_4$ seed crystals, all joints solidified with a single βSn orientation, though both Ag and Cu solute were present. In these specific cases, the joint sizes are much bigger than the Sn droplets used here and the Ag and Cu

concentrations are changed due to the dissolution of the Cu substrate. Further studies are needed to investigate these other factors that promote twinning of βSn.

It has been found here that Cu_6Sn_5, Ni_3Sn_4, and Ag_3Sn can act as heterogeneous nucleation sites for βSn (Figure 4, Figure 6, and Figure 8) with preferred ORs (Table 2) unless more catalytic sites are available (Table 3). Many of the droplets on these IMCs formed microstructures that are analogous to those widely reported in Sn-Ag and Sn-Ag-Cu solder joints on Cu or Ni substrates [1, 3-8, 56-61]. For example, the single-grain, cyclically-twinned and interlaced-twinned structures in the droplets in Figure 4, Figure 6, and Figure 8. This confirms that the droplet technique used here recreates phenomena that occur in solder joints. In these twinned droplets, it was common for one of the βSn grains to have the OR in Eq. 3, 4, 5 or 6 with the IMC facet. For example, in Figure 5 (A) grain 1 (marked with an asterisk) has the OR in Eq. 3 with Cu_6Sn_5, indicating that βSn both nucleated heterogeneously on the Cu_6Sn_5 facet, and developed into cyclic-twins.

Some droplets developed twinned structures that were complex, with heterogeneous nucleation on an IMC facet and multiple βSn orientations all linked by multiple rings of interrelated cyclic twins; For example, Figure 12 (B) shows five interrelated rings of cyclic-twins in a droplet on Ag_3Sn. The βSn grain labelled 1* has the OR in Eq. 5 and grains 2* and 3* have the OR in Eq. 6 indicating heterogeneous nucleation on the Ag_3Sn facet and grains 1, 2, 3, 4, 5, 6, 7 and 8 all have twin relationships indicated by the arrows and rings. Since all grains are interrelated by ~60° rotations around shared ~<100> axes, they almost certainly all come from a single nucleation event. These interrelated twinned structures are significantly more complex than those that form from the proposed twinned-nucleus model in ref. [1].

4 CONCLUSIONS

A droplet solidification technique has been applied to study the heterogeneous nucleation of βSn on single crystal intermetallic compounds and to extract new insights into cyclic twinning in solder solidification. The following conclusions can be drawn:

1. In Sn droplets on relatively potent IMCs ($\alpha CoSn_3$, $\beta IrSn_4$, $PdSn_4$, and $PtSn_4$), βSn nucleated on the IMC facet with a simple orientation relationship (OR) in every droplet even when the undercooling was relatively high. Crystallographically similar ORs formed on $\alpha CoSn_3$, $\beta IrSn_4$, $PdSn_4$, and $PtSn_4$. In the case of $PdSn_4$, the OR can be written:

   $(010)_{PdSn4}||(100)_{Sn}$ and $[100]_{PdSn4}||[001]_{Sn}$ or $[001]_{PdSn4}||[001]_{Sn}$

2. In Sn droplets on lower potency IMCs (Cu_6Sn_5, Ni_3Sn_4, and Ag_3Sn), βSn nucleated on the IMC facet in some droplets and not in others, indicating a competition between different low potency nucleation sites such as the IMC facet, impurity particles, and the oxide. When βSn nucleated on the IMC facet, the following preferred ORs were measured:

   $(10\bar{1}0)_{Cu6Sn5}||(111)_{Sn}$ and $[0001]_{Cu6Sn5}||[11\bar{2}]_{Sn}$

   $(100)_{Ni3Sn4}||(\bar{2}\bar{4}\bar{1})_{Sn}$ and $[0\bar{1}0]_{Ni3Sn4}||[10\bar{2}]_{Sn}$

   $(001)_{Ag3Sn}||(001)_{Sn}$ or $(001)_{Ag3Sn}||(301)_{Sn}$ both with $[010]_{Ag3Sn}||[010]_{Sn}$

   All ORs formed with misorientations in the parallel planes/directions within ~4° except for Ag_3Sn which had misorientations >10° in the parallel planes.

3. Cyclic twinning occurred in some Sn droplets solidified on the facets of Cu_6Sn_5, Ni_3Sn_4 or Ag_3Sn, with microstructures similar to those reported in electronic solder joints. In many cases there was both heterogeneous nucleation on the IMC facet (with a reproducible OR) and cyclic twinning. In the case of Cu_6Sn_5 and Ni_3Sn_4, only one of the twinned βSn grains had a simple OR with the IMC. For Ag_3Sn, all three cyclically twinned grains had one of two ORs all with a similar lattice match to the Ag_3Sn facet.

4. For twinned Sn droplets on Cu_6Sn_5, Ni_3Sn_4 or Ag_3Sn, the $<100>_{Sn}$ twinning axis always corresponded to the lowest linear disregistry on the IMC facet.

5. In twinned βSn droplets on Cu_6Sn_5 and Ni_3Sn_4, it was common for the twinning angles to be distinctly separable with one /two grains close to {101} twinning (57.2°) and the other(s) close to {301} twinning (62.8°).

6. While past work has reported single cyclic twins in solder joints, this work often measured both (i) an OR with the IMC particle and (ii) multiple interrelated cyclic twins in droplets, that have multiple shared <100> axes with cyclic twinning around each shared <100> axis. Up to 5 interrelated twinning axes were measured in a single droplet.

Acknowledgements

ZLM gratefully acknowledges the China Scholarship Council (CSC) (201306250005) for financial support through the Imperial-CSC scholarship scheme. CMG, SAB and JWX gratefully acknowledge funding from Nihon Superior Co., Ltd. and the UK EPSRC [grant numbers EP/M002241/1 and EP/N007638/1 (the EPSRC Future LiME Hub)].

Figure titles:

Figure 1 (A) A schematic phase diagram showing the Sn rich side of Sn-X systems (X= Co, Pt, Pd, Ir, Cu, Ni, Ag). The peak temperature for reflow is 240°C. (B) A schematic showing the possible nucleation mechanisms in the Sn droplet on the IMC.

Figure 2 (A) Single crystals of $\alpha CoSn_3$, $PtSn_4$, $PdSn_4$, and $\beta IrSn_4$ with facets indexed by EBSD. (B) A Sn droplet solidified on the (100) facet of $\alpha CoSn_3$. (C) 5 typical Sn droplets solidified on the (010) facet of a $PdSn_4$. (D) IPF-Y map. (E) Pole figures. βSn unit cell wireframes have the same colour as the EBSD maps. Triangles, circles, and squares indicate ORs between the βSn and the $PdSn_4$. (F) The summarised pole figure of βSn orientations in Sn droplets on $PdSn_4$ (see reference coordinate systems).

Figure 3 Nucleation undercoolings of ~40-75μm (Sn droplet size) single Sn droplets on IMCs (grey bars) and the ~550μm Sn-X alloy balls (red bars). For simplicity, only IMC names are shown to represent both droplets and alloys.

Figure 4 (A) A Cu_6Sn_5 crystal indexed as hexagonal ηCu_6Sn_5 [40] by EBSD. (B) The same crystal 70° tilted to the electron beam direction. (C) Typical Sn droplets on a Cu_6Sn_5 crystal, and grain orientations are shown individually using unit cell wireframes and dash lines. (D) EBSD IPF-X map region in (C). (E) Pole figures of droplet 4, droplet 6, and the Cu_6Sn_5 crystal. Parallel planes and directions are indicated by the same symbols, triangles indicate the facet of the Cu_6Sn_5 and parallel plane in βSn. Orientations of 37 βSn grains with the OR with Cu_6Sn_5 in Eq. 3 summarised into pole figures of (F) planes and (G) directions with respect to the orientation of the Cu_6Sn_5 (see the reference coordinate system). Blue text in (G) are selected linear disregistries.

Figure 5 (A) A Sn droplet on Cu_6Sn_5 (droplet 3 in Figure 4) showing 3 interrelated cyclic twins. All grains are labelled by numbers. The asterisked number indicates the grain that has the OR in Eq. 3 with Cu_6Sn_5. (B) The <100>Sn pole figure of the Sn droplet showing how the 3 cyclic twins are related. (C) Translated βSn unit cell wireframes of 3 cyclic twins arranged in either {101} or {301} cyclic twinning type. Dashed unit cells were not measured but are shown for clarity. Red, green and blue are used to indicate twinning axes and shared common planes. (D) The misorientations δ_{ij} between twinning axes, the in-grain misorientation m_i, and the misorientation ω_{ij} between the other <100> axes of grains in twins i. (E) Angular distributions of misorientation between grains in twins i.

Figure 6 (A) A Ni_3Sn_4 crystal indexed as *mS14*-Ni_3Sn_4 [41] by EBSD. (B) The same crystal 70° tilted to the electron beam direction. (C) Typical Sn droplets on Ni_3Sn_4. Grain orientations are shown on each Sn droplet as unit cell wireframes. (D) EBSD IPF-X map. (E) Pole figures of droplet 1 and the Ni_3Sn_4 crystal. Parallel planes and directions in βSn and Ni_3Sn_4 are indicated by the same symbols. Triangles indicate the facet of Ni_3Sn_4 and parallel plane in βSn. (F,G) βSn grains with the OR in Eq. 4 summarised into a pole figure with respect to Ni_3Sn_4 (see the reference coordinate system). (F) Planes. (G) Directions. Blue text in (G) are selected linear disregistries.

Figure 7 (A) Atomic matching between βSn and Ni_3Sn_4 on different facets. (B) Planar atomic matching of interfaces on the three facets. All near-interface atoms are projected into the plane. Transparent atoms are out of plane.

Figure 8 (A) A typical Ag_3Sn single crystal indexed as *oP8*-Ag_3Sn [42] by EBSD. (B) The same crystal that is 54° tilted to the electron beam direction. (C) Typical Sn droplets on Ag_3Sn, with βn orientations shown with unit cell wireframes. (D) EBSD IPF-Z map. (E) Pole figures of droplet 8 and the Ag_3Sn crystal. To represent the OR, parallel planes and directions in the βSn and the Ag_3Sn are indicated by the same symbols. Triangles indicate the facet of the Ag_3Sn and corresponding parallel

plane in βSn. (F) Orientations of βSn grains that have the ORs in Eq. 5 and Eq. 6 with Ag_3Sn summarised into pole figures with respect to Ag_3Sn (see the reference coordinate system).

Figure 9 (A) A typical droplet on Ag_3Sn with interlaced-twinned βSn structure with an EBSD IPF-Z map and unit cell wireframes superimposed. (B) Corresponding pole figures with parallel planes and directions labelled using the same symbols. (C) The OR between cyclic twinned βSn grains and Ag_3Sn created by translating the unit cells and rotating all orientations in (A) 90° upwards (see their coordinate systems). Parallel planes in βSn and Ag_3Sn are indicated by black shaded planes. Red planes indicate the common plane of cyclic twinned βSn grains. (D) Misorientations δ_{ij} between twinning axes, in-grain misorientation m_i, and the misorientation ω_{ij} between the other <100> axes of grains. (E) Angular distributions of misorientation between grains in the interlaced twins.

Figure 10 (A) Atomic matching between βSn and Ag_3Sn in (A) OR in Eq. 5 and (C) OR in Eq. 6. (B) and (D) The corresponding interfacial atomic match shown by projecting all near-interface atoms into the plane. Transparent atoms are out of plane.

Figure 11 Interfaces of Sn droplets on IMCs after dissolving all βSn: (A) $\alpha CoSn_3$, (B) $PdSn_4$, (C) $\beta IrSn_4$, (D) $PtSn_4$, (E) Cu_6Sn_5, (F) Ni_3Sn_4, and (G) Ag_3Sn. (H)-(K) FIB-tomography of the Sn droplet on Ag_3Sn in Figure 9: (H) the secondary electron image, (I) reconstructed tin droplet, (J) the interface on Ag_3Sn, and (K) a semi-transparent side view showing the wetting angle and the average dissolved thickness of the Ag_3Sn single crystal.

Figure 12 (A) A Sn-3.0Ag-0.5Cu droplet on a (100)$\alpha CoSn_3$ facet and the EBSD IPF-Z map of βSn in this droplet. The orientations of the cyclic twinned βSn grains are shown in the {101} type twinning configuration. (B) A Sn droplet on a (001)Ag_3Sn facet showing 5 interrelated twins as indicated by the superimposed βSn unit cell wireframes and coloured twinning axes. Arrows show orientations that are shared between two rings of cyclic twins.

Tables:

Table 1 Crystal structures and lattice parameters used for indexing EBSD patterns (fractional coordinates are in the references).

Phase	Space group	Pearson symbol	Lattice parameters						Ref.
			a(nm)	b(nm)	c(nm)	α(°)	β(°)	γ(°)	
βSn	*I4₁/amd*	*tI4*	0.5831	0.5831	0.3182	90	90	90	[35]
$PtSn_4$	*Ccca*	*oS*20	0.6418	1.1366	0.6384	90	90	90	[36]
$PdSn_4$	*Ccca*	*oS*20	0.6442	1.1445	0.6389	90	90	90	[37]
$\alpha CoSn_3$	*Cmca*	*oS*32	1.6864	0.6268	0.6270	90	90	90	[38]
$\beta IrSn_4$	*I4₁/acd*	*tI*40	0.6310	0.6310	2.2770	90	90	90	[39]
ηCu_6Sn_5	*P6₃/mmc*	*hP*4	0.4206	0.4206	0.5097	90	90	120	[40]
Ni_3Sn_4	*C*2/*m*	*mS*14	1.2214	0.4060	0.5219	90	105	90	[41]
Ag_3Sn	*Pmmn*	*oP*8	0.4782	0.5998	0.5164	90	90	90	[42]

Table 2 Summary of main IMC facets, measured parallel planes in βSn, common directions on planes, the frequency of occurrence of each OR, and the nucleation undercooling of single Sn droplets on the IMC. The $\alpha CoSn_3$, $PtSn_4$, and $IrSn_4$ data are from ref. [28].

IMC	IMC facets	Parallel plane in βSn	Common directions on planes	Frequency of occurrence	ΔT_{nuc} (K)
$\alpha CoSn_3$	(100)	(100)	$[010]CoSn_3\|\|[001]Sn$	16 out of 41	14 ± 4
			$[001]CoSn_3\|\|[001]Sn$	25 out of 41	
$PtSn_4$	(010)	(100)	$[100]PtSn_4\|\|[001]Sn$	93 out of 105	29 ± 8
			$[001]PtSn_4\|\|[001]Sn$	12 out of 105	
$PdSn_4$	(010)	(100)	$[100]PdSn_4\|\|[001]Sn$	73 out of 117	21 ± 6
			$[001]PdSn_4\|\|[001]Sn$	44 out of 117	
$\beta IrSn_4$	(001)	(100)	$[100]IrSn_4\|\|[001]Sn$	36 out of 36	19 ± 3
Cu_6Sn_5	$\{10\bar{1}0\}$	(241)	$[0001]Cu_6Sn_5\|\|[1\bar{1}2]Sn$	32 out of 60	53 ± 11
		$(\bar{1}11)$	$[0001]Cu_6Sn_5\|\|[1\bar{1}2]Sn$	5 out of 60	
Ni_3Sn_4	(100)	[a](241)	$[010]Ni_3Sn_4\|\|[\bar{1}02]Sn$	82 out of 111	35 ± 5
	(001)	[a](211)	$[010]Ni_3Sn_4\|\|[\bar{1}02]Sn$	16 out of 47	
	$(\bar{2}01)$	[a](261)	$[010]Ni_3Sn_4\|\|[\bar{1}02]Sn$	14 out of 21	
Ag_3Sn	(001)	(001)	$[010]Ag_3Sn\|\|[010]Sn$	[b]3+140 out of 188	39 ± 8
		(301)	$[010]Ag_3Sn\|\|[010]Sn$	[b]2+140 out of 188	

a. The parallel βSn planes with Ni_3Sn_4 facets are different, but represent the same OR (see Eq. 4)

b. A+B means that there are A droplets that show single grain and only have this OR, and B droplets that contain grains with both $(001)Ag_3Sn||(001)Sn$ and $(001)Ag_3Sn||(301)Sn$.

Table 3 Summary of βSn microstructures in Sn droplets on IMC facets. Gs=grains, Ts=twins, IGs= independent grains.

IMC	Facet	Parallel plane in βSn	Sum	Sn droplet microstructure and frequency of occurrence									
				Single grain	Simple twins		Interlaced twins		Interrelated twins				Multiple IGs
					2 Gs	3 Gs	2 Gs	3 Gs	2 Ts	3 Ts	4 Ts	>4 Ts	
$\alpha CoSn_3$	(100)	(100)	41	41	--	--	--	--	--	--	--	--	--
$PtSn_4$	(010)	(100)	105	105	--	--	--	--	--	--	--	--	--
$PdSn_4$	(010)	(100)	117	117	--	--	--	--	--	--	--	--	--
$\beta IrSn_4$	(001)	(100)	36	36	--	--	--	--	--	--	--	--	--
Cu_6Sn_5	$\{10\bar{1}0\}$	(241)	32	11	--	3	--	--	4	3	2	2	7
		(111)	5	--	--	1	--	--	2	--	--	--	2
		Others	23	13	1	3	--	--	--	--	--	--	6
Ni_3Sn_4	(100)	(241)	82	54	9	9	1	--	6	--	--	--	3
		Others	29	21	1	2	--	--	1	--	--	--	4
	(001)	(211)	16	10	1	1	--	--	--	--	--	--	4
		Others	31	20	1	--	--	--	2	--	--	--	8
	$(\bar{2}01)$	(261)	14	10	2	1	--	--	--	--	--	--	1
		Others	7	7	--	--	--	--	--	--	--	--	--
Ag_3Sn	(001)	(001)	143	3	6	3	8	50	17	1	3	4	48
		(301)	142	2	6	3	8	50	17	1	3	4	48
		Others	43	15	7	2	--	--	--	--	--	--	19

Table 4 Planes and atomic rows ranked by atomic density (nm^{-2}) and interatomic distance (nm) for βSn, Cu_6Sn_5, Ni_3Sn_4, and Ag_3Sn. N.B. some planes and directions are zig-zag and calculations have projected all atoms into the planes/directions.

Rank	βSn (tetragonal)		ηCu_6Sn_5 (hexagonal)		Ni_3Sn_4 (monoclinic)		Ag_3Sn (orthorhombic)	
	Plane, [a]PD	Direction, [b]AD	Plane, [a]PD	Direction, [b]AD	Plane, [a]PD	Direction, [b]AD	Plane, [a]PD	Direction, [b]AD
1	{100}, 10.78	<100>, 0.292	$\{0\bar{2}\bar{2}2\}$, 11.87	<0001>, 0.255	{111}, 12.32	<001>, 0.261	{100}, 12.91	<010>, 0.300
2	{110}, 7.62	<001>, 0.318	$\{\bar{2}110\}$, 11.85	$<2\bar{2}01>$, 0.257	$\{3\bar{1}\bar{2}\}$, 11.66	$<10\bar{1}>$, 0.290	{121}, 12.52	<101>, 0.352
3	{211}, 7.46	<101>, 0.332	$\{10\bar{1}0\}$, 9.34	$<1\bar{1}01>$, 0.296	$\{\bar{4}01\}$, 11.57	<154>, 0.294	{102}, 12.27	<100>, 0.478
4	{241}, 5.45	<102>, 0.432	{0004}, 7.83	$<10\bar{1}0>$, 0.364	{010}, 11.37	<203>, 0.362	{010}, 8.10	<001>, 0.516
5	{111}, 4.66	<111>, 0.442	--	$<2\bar{1}\bar{1}0>$, 0.421	{001}, 8.07	<010>, 0.406	{001}, 6.97	<201>, 0.544
6	{201}, 3.97	<103>, 0.559	--	$<2\bar{1}\bar{1}3>$, 0.661	$\{\bar{2}01\}$, 7.11	<130>, 0.862		
7	{261}, 3.27	<104>, 0.700	--		{100}, 4.72	<100>, 1.221	--	--
8	{221}, 3.20	<112>, 1.042	--	--	--	--	--	--
9	{001}, 2.94	<412>, 1.244	--	--	--	--	--	--

a Planar atomic density, nm^{-2}. The ranking goes down when the density decreases.

b Atomic distance, nm. The ranking goes down when the distance increases (i.e. less close packed).

Table 5 Changes in liquid composition, volume fractions of primary and eutectic IMC, and dissolved thickness of the main IMC crystal for the situation in Figure 1. Calculation details are given in the Supplementary Information.

Sn/IMC	[a] C_E (wt%)	[a] $C_L(240)$ (wt%)	[b] C_{IMC} (wt%)	[c] Density ($g \cdot cm^{-3}$)	[d] f_{IMC}^{pri} (vol%)	[e] f_{IMC}^{eut} (vol%)	[f] Δh (nm)
βSn	--	--	--	7.26	--	--	--
$\alpha CoSn_3$	0.02 Co	0.02 Co	14.2 Co	8.32	0.03	0.09	3
$PtSn_4$	0.03 Pt	0.03 Pt	29.1 Pt	9.55	0.08	0.002	2
$PdSn_4$	0.40 Pd	0.52 Pd	18.3 Pd	8.20	1.45	1.07	57
$\beta IrSn_4$	--	--	28.8 Ir	9.79	--	--	--
Cu_6Sn_5	0.89 Cu	1.08 Cu	39.1 Cu	8.31	1.63	0.42	55
Ni_3Sn_4	0.04 Ni	0.04 Ni	27.1 Ni	8.65	0.06	0.07	3
Ag_3Sn	3.73 Ag	4.70 Ag	73.2 Ag	9.92	2.89	2.52	110

a C_E (the eutectic composition of Sn-IMC) and C_L data are from ref. [62], except C_E of Pt-Sn from [47].

b C_{IMC} is the composition of the IMC, assuming stoichiometric compounds.

c Densities are theoretical values for the crystals in Table 1.

d Volume % of primary IMC, assuming the nucleation undercooling in Table 2.

e Volume % of eutectic IMC, assuming the nucleation undercooling in Table 2.

f Thickness dissolved in Figure 1 (B), assuming a droplet diameter d = 20μm, wetting angle θ = 20°.

References

[1] L.P. Lehman, Y. Xing, T.R. Bieler, E.J. Cotts. Cyclic twin nucleation in tin-based solder alloys, Acta Mater 58 (2010) 3546-3556.
[2] B. Arfaei, N. Kim, E.J. Cotts. Dependence of Sn Grain Morphology of Sn-Ag-Cu Solder on Solidification Temperature, J Electron Mater 41 (2012) 362-374.
[3] C.M. Gourlay, S.A. Belyakov, Z.L. Ma, J.W. Xian. Nucleation and Growth of Tin in Pb-Free Solder Joints, JOM 67 (2015) 2383-2393.
[4] Z.L. Ma, S.A. Belyakov, C.M. Gourlay. Effects of cobalt on the nucleation and grain refinement of Sn-3Ag-0.5Cu solders, J Alloy Compd 682 (2016) 326-337.
[5] Z.L. Ma, C.M. Gourlay. Nucleation, grain orientations, and microstructure of Sn-3Ag-0.5Cu soldered on cobalt substrates, J Alloy Compd 706 (2017) 596-608.
[6] J.W. Xian, Z.L. Ma, S.A. Belyakov, M. Ollivier, C.M. Gourlay. Nucleation of tin on the Cu6Sn5 layer in electronic interconnections, Acta Mater 123 (2017) 404-415.
[7] S.-K. Seo, S.K. Kang, M.G. Cho, D.-Y. Shih, H.M. Lee. The Crystal Orientation of β-Sn Grains in Sn-Ag and Sn-Cu Solders Affected by Their Interfacial Reactions with Cu and Ni(P) Under Bump Metallurgy, J Electron Mater 38 (2009) 2461-2469.
[8] S.-K. Seo, S.K. Kang, D.-Y. Shih, H.M. Lee. An Investigation of Microstructure and Microhardness of Sn-Cu and Sn-Ag Solders as Functions of Alloy Composition and Cooling Rate, J Electron Mater 38 (2009) 257-265.
[9] K.N. Reeve, C.A. Handwerker. Beta-Tin Grain Formation in Aluminum-Modified Lead-Free Solder Alloys, J Electron Mater (2017).
[10] H. Shang, Z.L. Ma, S.A. Belyakov, C.M. Gourlay. Grain refinement of electronic solders: The potential of combining solute with nucleant particles, J Alloy Compd 715 (2017) 471-485.
[11] L. Lehman, R. Kinyanjui, J. Wang, Y. Xing, L. Zavalij, P. Borgesen, E. Cotts. Microstructure and damage evolution in Sn-Ag-Cu solder joints. Electronic Components and Technology Conference, 2005. Proceedings. 55th: IEEE, 2005. p.674-681.
[12] B. Arfaei, L. Wentlent, S. Joshi, A. Alazzam, T. Tashtoush, M. Halaweh, S. Chivukula, L. Yin, M. Meilunas, E. Cotts, P. Borgesen. Improving the thermomechanical behavior of lead free solder joints by controlling the microstructure. Thermal and Thermomechanical Phenomena in Electronic Systems (ITherm), 13th IEEE Intersociety Conference, 2012. p.392-398.
[13] I.E. Anderson, J.C. Foley, B.A. Cook, J. Harringa, R.L. Terpstra, O. Unal. Alloying effects in near-eutectic Sn-Ag-Cu solder alloys for improved microstructural stability, J Electron Mater 30 (2001) 1050-1059.
[14] I.E. Anderson. Development of Sn-Ag-Cu and Sn-Ag-Cu-X alloys for Pb-free electronic solder applications, J Mater Sci-Mater El 18 (2007) 55-76.
[15] K.S. Kim, S.H. Huh, K. Suganuma. Effects of fourth alloying additive on microstructures and tensile properties of Sn–Ag–Cu alloy and joints with Cu, Microelectron Reliab 43 (2003) 259-267.
[16] L. Sun, L. Zhang. Properties and Microstructures of Sn-Ag-Cu-X Lead-Free Solder Joints in Electronic Packaging, Adv Mater Sci Eng 2015 (2015) 16.
[17] O. Krammer, T. Garami. Reliability investigation of low silver content micro-alloyed SAC solders. Electronics Technology (ISSE), 35th International Spring Seminar on Electronics Technology, 2012. p.149-154.
[18] J. Mao, B. Reeves, B. Lenz, D. Ruscitto, D. Lewis. Study on the Effect of Mn, Zn, and Sb on Undercooling Behavior of Sn-Ag-Cu Alloys Using Differential Thermal Analysis, J Electron Mater 46 (2017) 6319-6332.
[19] I.E. Anderson, J. Walleser, J.L. Harringa. Observations of nucleation catalysis effects during solidification of SnAgCuX solder joints, JOM 59 (2007) 38-43.
[20] Y.C. Huang, S.W. Chen, K.S. Wu. Size and Substrate Effects upon Undercooling of Pb-Free Solders, J Electron Mater 39 (2010) 109-114.
[21] S. Chada, R.A. Fournelle, W. Laub, D. Shangguan. Copper substrate dissolution in eutectic Sn-Ag solder and its effect on microstructure, J Electron Mater 29 (2000) 1214-1221.

[22] M. Huang, F. Yang. Size effect model on kinetics of interfacial reaction between Sn-xAg-yCu solders and Cu substrate, Sci Rep 4 (2014).
[23] N. Dariavach, P. Callahan, J. Liang, R. Fournelle. Intermetallic growth kinetics for Sn-Ag, Sn-Cu, and Sn-Ag-Cu lead-free solders on Cu, Ni, and Fe-42Ni substrates, J Electron Mater 35 (2006) 1581-1592.
[24] K.S. Kim, S.H. Huh, K. Suganuma. Effects of intermetallic compounds on properties of Sn-Ag-Cu lead-free soldered joints, J Alloy Compd 352 (2003) 226-236.
[25] R.K. Chinnam, C. Fauteux, J. Neuenschwander, J. Janczak-Rusch. Evolution of the microstructure of Sn–Ag–Cu solder joints exposed to ultrasonic waves during solidification, Acta Mater 59 (2011) 1474-1481.
[26] B. Arfaei, E. Cotts. Correlations Between the Microstructure and Fatigue Life of Near-Eutectic Sn-Ag-Cu Pb-Free Solders, J Electron Mater 38 (2009) 2617-2627.
[27] D.W. Henderson, T. Gosselin, A. Sarkhel, S.K. Kang, W.K. Choi, D.Y. Shih, C. Goldsmith, K.J. Puttlitz. Ag3Sn plate formation in the solidification of near ternary eutectic Sn-Ag-Cu alloys, J Mater Res 17 (2002) 2775-2778.
[28] Z.L. Ma, S.A. Belyakov, K. Sweatman, T. Nishimura, T. Nishimura, C.M. Gourlay. Harnessing heterogeneous nucleation to control tin orientations in electronic interconnections, Nat Commun 8 (2017) 1916.
[29] I.E. Anderson, J.W. Walleser, J.L. Harringa, F. Laabs, A. Kracher. Nucleation Control and Thermal Aging Resistance of Near-Eutectic Sn-Ag-Cu-X Solder Joints by Alloy Design, J Electron Mater 38 (2009) 2770-2779.
[30] Z.G. Chen, Y.W. Shi, Z.D. Xia, Y.F. Yan. Study on the microstructure of a novel lead-free solder alloy SnAgCu-RE and its soldered joints, J Electron Mater 31 (2002) 1122-1128.
[31] S.H. Yang, Y.H. Tian, C.Q. Wang. Investigation on Sn grain number and crystal orientation in the Sn-Ag-Cu/Cu solder joints of different sizes, J Mater Sci-Mater El 21 (2010) 1174-1180.
[32] M.G. Cho, S.K. Kang, S.-K. Seo, D.-Y. Shih, H.M. Lee. Effects of under bump metallization and nickel alloying element on the undercooling behavior of Sn-based, Pb-free solders, J Mater Res 24 (2009) 534-543.
[33] D. Turnbull. Kinetics of Heterogeneous Nucleation, J Chem Phys 18 (1950) 198-203.
[34] J.H. Perepezko, M.J. Uttormark. Nucleation-Controlled Solidification Kinetics, Metall Mater Trans A 27 (1996) 533-547.
[35] H.E. Swanson, H.F. McMurdie, M.C. Morris, E.H. Evans, B. Paretzkin. Standard X-ray diffraction powder patterns, Nat Bur Stand(U.S.) 569 (1953) 1-95.
[36] B. Künnen, D. Niepmann, W. Jeitschko. Structure refinements and some properties of the transition metal stannides Os3Sn7, Ir5Sn7, Ni0.402(4)Pd0.598Sn4, α-PdSn2 and PtSn4, J Alloy Compd 309 (2000) 1-9.
[37] J. Nylén, F.J. Garcìa Garcìa, B.D. Mosel, R. Pöttgen, U. Häussermann. Structural relationships, phase stability and bonding of compounds PdSnn (n=2, 3, 4), Solid State Sci 6 (2004) 147-155.
[38] A. Lang, W. Jeitschko. Two new phases in the system cobalt-tin: the crystal structures of a- and ß-CoSn3, Z Metallkd 87 (1996) 759-764.
[39] E.-L. Nordmark, O. Wallner, U. Häussermann. Polymorphism of IrSn4, J Solid State Chem 168 (2002) 34-40.
[40] B. Peplinski, G. Schulz, D. Schultze, E. Schierhorn. Improved X-ray powder diffraction data for the disordered η-Cu6Sn5 alloy phase. Mater Sci Forum, vol. 228: Trans Tech Publ, 1996. p.577-582.
[41] W. Jeitschko, B. Jaberg. Structure refinement of Ni3Sn4, Acta Crystall B: Stru 38 (1982) 598-600.
[42] P.J. Rossi, N. Zotov, E.J. Mittemeijer. Redetermination of the crystal structure of the Ag3Sn intermetallic compound, Z Kristallogr Crystallogr Mater 231 (2016) 1-9.
[43] Y.Q. Wu, J.C. Barry, T. Yamamoto, Q.F. Gu, S.D. McDonald, S. Matsumura, H. Huang, K. Nogita. A new phase in stoichiometric Cu6Sn5, Acta Mater 60 (2012) 6581-6591.

[44] A.-K. Larsson, L. Stenberg, S. Lidin. The superstructure of domain-twinned η'-Cu6Sn5, Acta Crystallogra B: Stru Sci 50 (1994) 636-643.
[45] S. Lidin, A.-K. Larsson. A Survey of Superstructures in Intermetallic NiAs-Ni2In-Type Phases, J Solid State Chem 118 (1995) 313-322.
[46] G. Ghosh, M. Asta. Phase Stability, Phase Transformations, and Elastic Properties of Cu6Sn5: Ab initio Calculations and Experimental Results, J Mater Res 20 (2005) 3102-3117.
[47] S.A. Belyakov, C.M. Gourlay. Heterogeneous nucleation of βSn on NiSn4, PdSn4 and PtSn4, Acta Mater 71 (2014) 56-68.
[48] J.W. Xian, S.A. Belyakov, T.B. Britton, C.M. Gourlay. Heterogeneous nucleation of Cu6Sn5 in Sn–Cu–Al solders, J Alloy Compd 619 (2015) 345-355.
[49] W. Liu, Y. Tian, C. Wang, X. Wang, R. Liu. Morphologies and grain orientations of Cu–Sn intermetallic compounds in Sn3.0Ag0.5Cu/Cu solder joints, Mater Lett 86 (2012) 157-160.
[50] Z.H. Zhang, H.J. Cao, H.F. Yang, M.Y. Li, Y.X. Yu. Hexagonal-Rod Growth Mechanism and Kinetics of the Primary Cu6Sn5 Phase in Liquid Sn-Based Solder, J Electron Mater 45 (2016) 5985-5995.
[51] J.W. Xian, S.A. Belyakov, M. Ollivier, K. Nogita, H. Yasuda, C.M. Gourlay. Cu6Sn5 crystal growth mechanisms during solidification of electronic interconnections, Acta Mater 126 (2017) 540-551.
[52] J.W. Xian, G. Zeng, S.A. Belyakov, Q. Gu, K. Nogita, C.M. Gourlay. Anisotropic thermal expansion of Ni3Sn4, Ag3Sn, Cu3Sn, Cu6Sn5 and βSn, Intermetallics 91 (2017) 50-64.
[53] P.M. Kelly, M.-X. Zhang. Edge-to-edge matching—The fundamentals, Metall Mater Trans A 37 (2006) 833-839.
[54] M.X. Zhang, P.M. Kelly, M.A. Easton, J.A. Taylor. Crystallographic study of grain refinement in aluminum alloys using the edge-to-edge matching model, Acta Mater 53 (2005) 1427-1438.
[55] H. Zou, H. Yang, J. Tan, Z. Zhang. Preferential growth and orientation relationship of Ag 3 Sn grains formed between molten Sn and (001) Ag single crystal, J Mater Res 24 (2009) 2141-2144.
[56] M. Lu, D.-Y. Shih, P. Lauro, C. Goldsmith, D.W. Henderson. Effect of Sn grain orientation on electromigration degradation mechanism in high Sn-based Pb-free solders, Appl Phys Lett 92 (2008) 211909.
[57] Y. Wang, K.H. Lu, V. Gupta, L. Stiborek, D. Shirley, S.-H. Chae, J. Im, P.S. Ho. Effects of Sn grain structure on the electromigration of Sn–Ag solder joints, J Mater Res 27 (2012) 1131-1141.
[58] G. Parks, B. Arfaei, M. Benedict, E. Cotts, L. Minhua, E. Perfecto. The dependence of the Sn grain structure of Pb-free solder joints on composition and geometry. IEEE 62th Electronic Components and Technology Conference 2012. p.703-709.
[59] M. Lu, P. Lauro, D.Y. Shih, R. Polastre, C. Goldsmith, D.W. Henderson, H. Zhang, C. Moon Gi. Comparison of electromigration performance for Pb-free solders and surface finishes with Ni UBM. IEEE 58th Electronic Components and Technology Conference, 2008. p.360-365.
[60] G. Parks, M. Lu, E. Perfecto, E. Cotts. Controlling the Sn grain morphology of SnAg C4 solder bumps. IEEE 64th Electronic Components and Technology Conference 2014. p.690-696.
[61] B. Arfaei, S. Mahin-Shirazi, S. Joshi, M. Anselm, P. Borgesen, E. Cotts, J. Wilcox, R. Coyle. Reliability and failure mechanism of solder joints in thermal cycling tests. IEEE 63rd Electronic Components and Technology Conference, 2013. p.976-985.
[62] Thermo-Calc. TCSLD Database version 3.0. 2015.

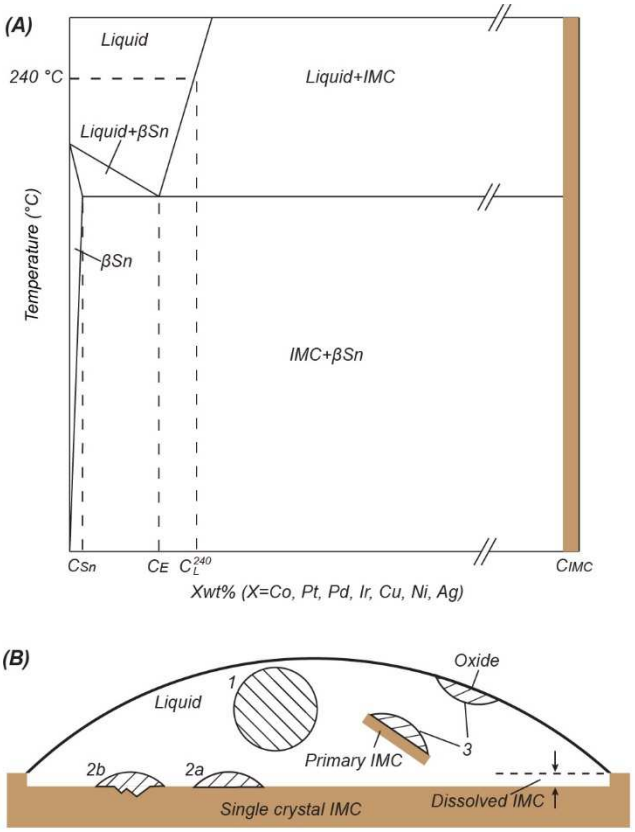

Figure 1 (A) A schematic phase diagram showing the Sn rich side of Sn-X systems (X= Co, Pt, Pd, Ir, Cu, Ni, Ag). The peak temperature for reflow is 240°C. (B) A schematic showing the possible nucleation mechanisms in the Sn droplet on the IMC.

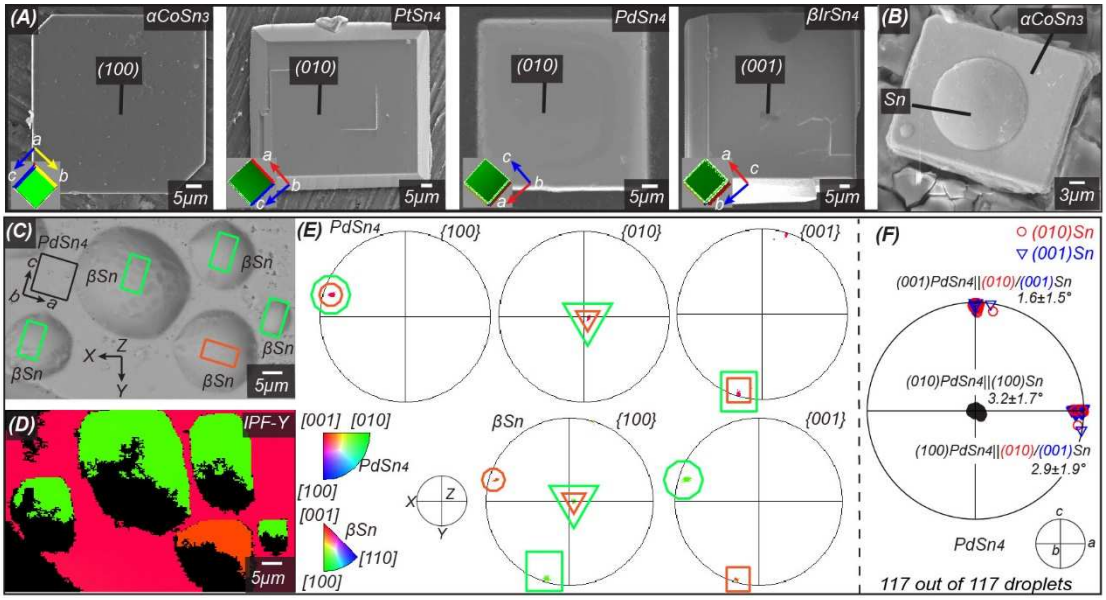

Figure 2 (A) Single crystals of $\alpha CoSn_3$, $PtSn_4$, $PdSn_4$, and $\beta IrSn_4$ with facets indexed by EBSD. (B) A Sn droplet solidified on the (100) facet of $\alpha CoSn_3$. (C) 5 typical Sn droplets solidified on the (010) facet of a $PdSn_4$. (D) IPF-Y map. (E) Pole figures. βSn unit cell wireframes have the same colour as the EBSD maps. Triangles, circles, and squares indicate ORs between the βSn and the $PdSn_4$. (F) The summarised pole figures of βSn orientations in Sn droplets on $PdSn_4$ (see reference coordinate systems).

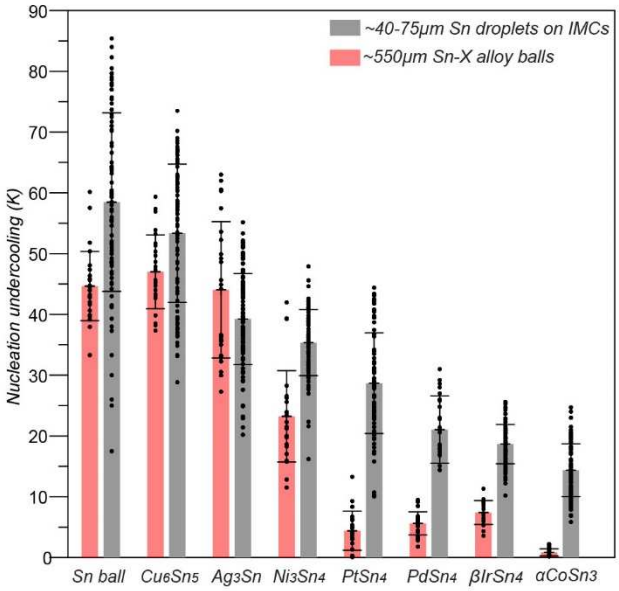

Figure 3 Nucleation undercoolings of ~40-75μm (Sn droplet size) single Sn droplets on IMCs (grey bars) and the ~550μm Sn-X alloy balls (red bars). For simplicity, only IMC names are shown to represent both droplets and alloys

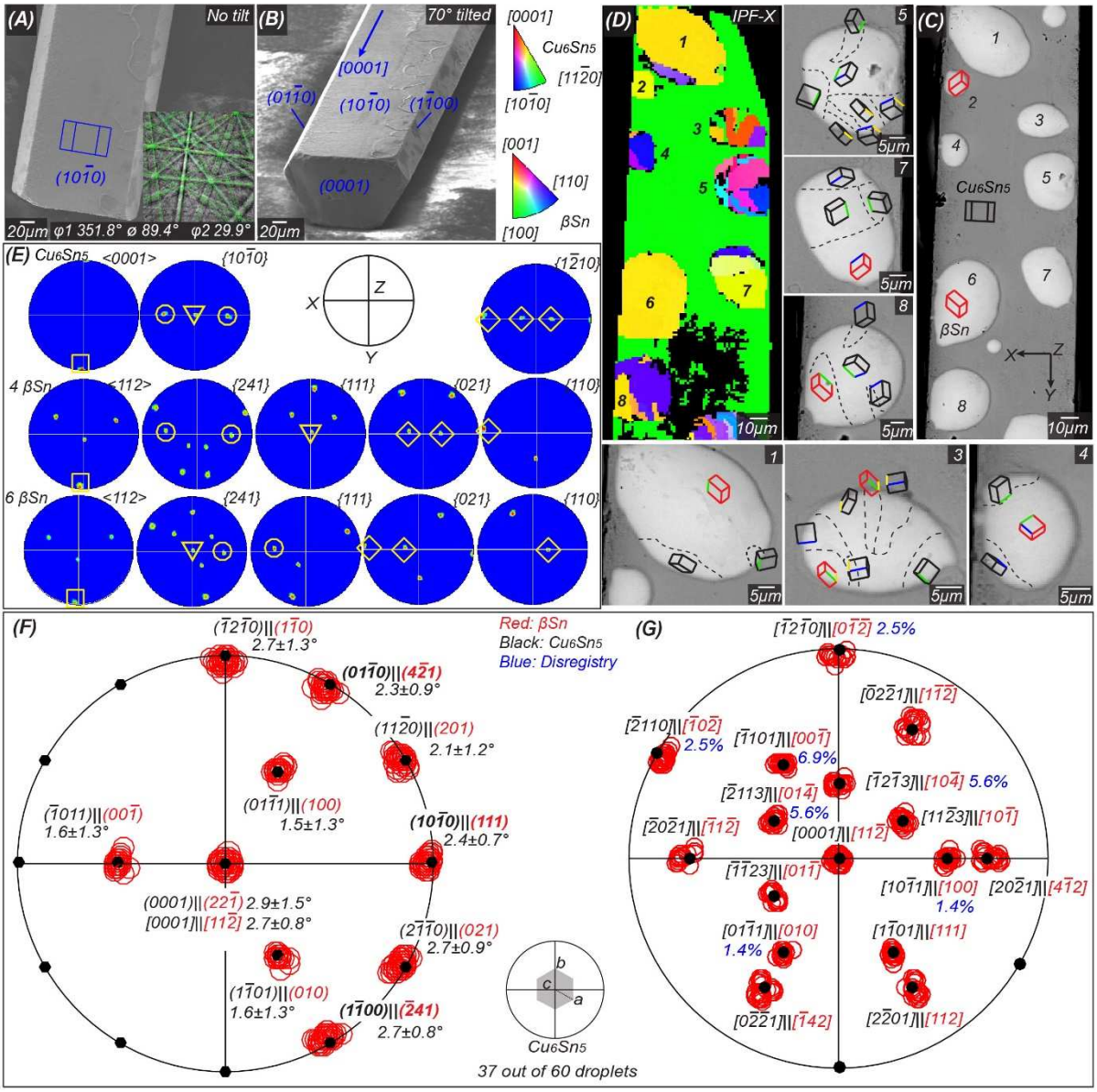

Figure 4 (A) A Cu_6Sn_5 crystal indexed as hexagonal ηCu_6Sn_5 [40] by EBSD. (B) The same crystal 70° tilted to the electron beam direction. (C) Typical Sn droplets on a Cu_6Sn_5 crystal, and grain orientations are shown individually using unit cell wireframes and dash lines. (D) EBSD IPF-X map region in (C). (E) Pole figures of droplet 4, droplet 6, and the Cu_6Sn_5 crystal. Parallel planes and directions are indicated by the same symbols, triangles indicate the facet of the Cu_6Sn_5 and parallel plane in βSn. Orientations of 37 βSn grains with the OR with Cu_6Sn_5 in Eq. 3 summarised into pole figures of (F) planes and (G) directions with respect to the orientation of the Cu_6Sn_5 (see the reference coordinate system). Blue text in (G) are selected linear disregistries.

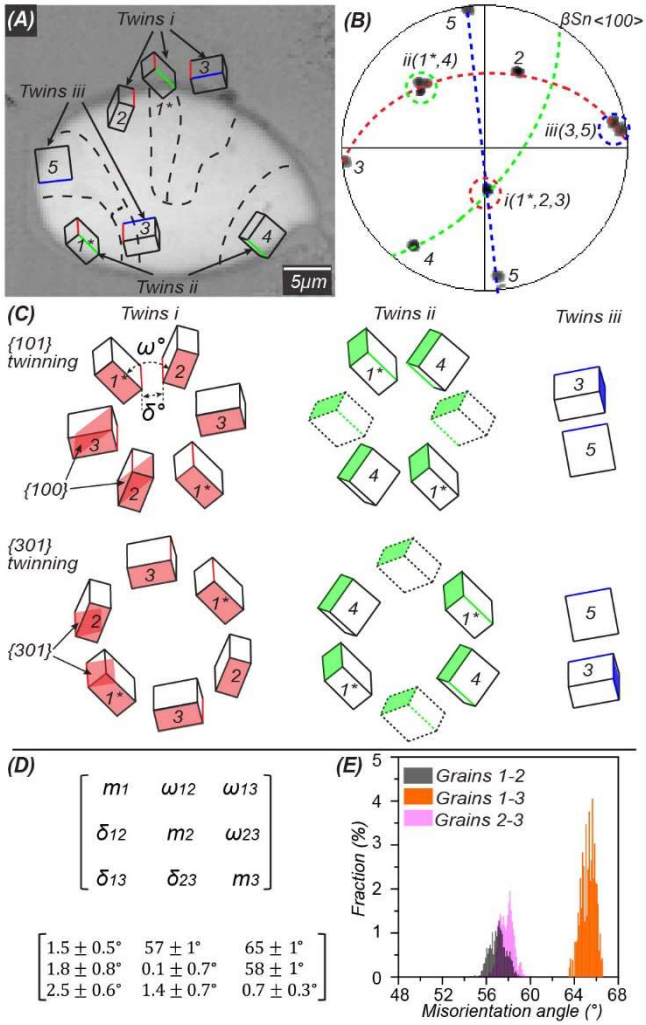

Figure 5 (A) A Sn droplet on Cu_6Sn_5 (droplet 3 in Figure 4) showing 3 interrelated cyclic twins. All grains are labelled by numbers. The asterisked number indicates the grain that has the OR in Eq. 3 with Cu_6Sn_5. (B) The <100>Sn pole figure of the Sn droplet showing how the 3 cyclic twins are related. (C) Translated βSn unit cell wireframes of 3 cyclic twins arranged in either {101} or {301} cyclic twinning type. Dashed unit cells were not measured but are shown for clarity. Red, green and blue are used to indicate twinning axes and shared common planes. (D) The misorientations δ_{ij} between twinning axes, the in-grain misorientation m_i, and the misorientation ω_{ij} between the other <100> axes of grains in twins i. (E) Angular distributions of misorientation between grains in twins i.

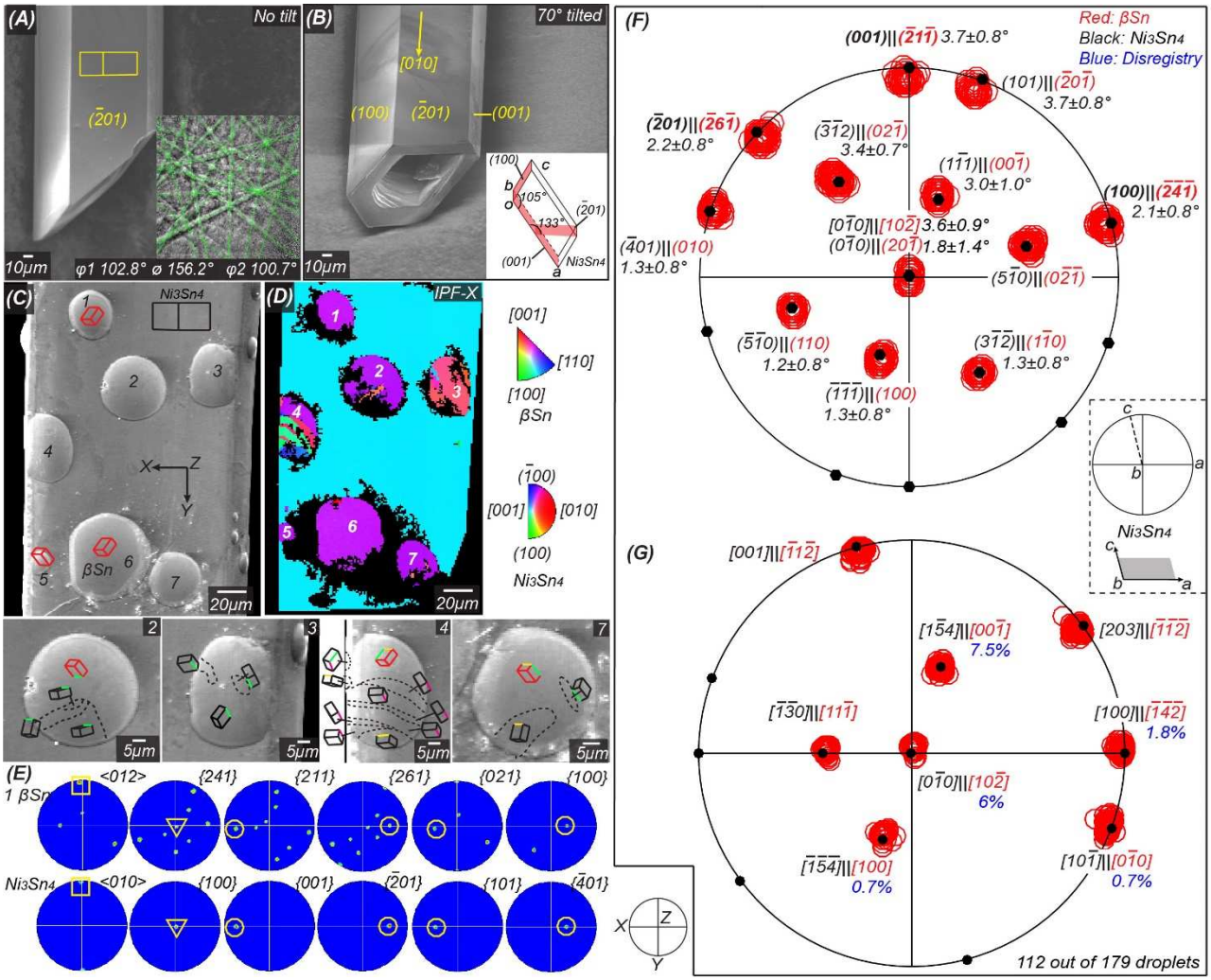

Figure 6 (A) A Ni_3Sn_4 crystal indexed as *mS14*-Ni_3Sn_4[41] by EBSD. (B) The same crystal 70° tilted to the electron beam direction. (C) Typical Sn droplets on Ni_3Sn_4. Grain orientations are shown on each Sn droplet as unit cell wireframes. (D) EBSD IPF-X map. (E) Pole figures of droplet 1 and the Ni_3Sn_4 crystal. Parallel planes and directions in βSn and Ni_3Sn_4 are indicated by the same symbols. Triangles indicate the facet of Ni_3Sn_4 and parallel plane in βSn. (F,G) βSn grains with the OR in Eq. 4 summarised into a pole figure with respect to Ni_3Sn_4 (see the reference coordinate system). (F) Planes. (G) Directions. Blue text in (G) are selected linear disregistries.

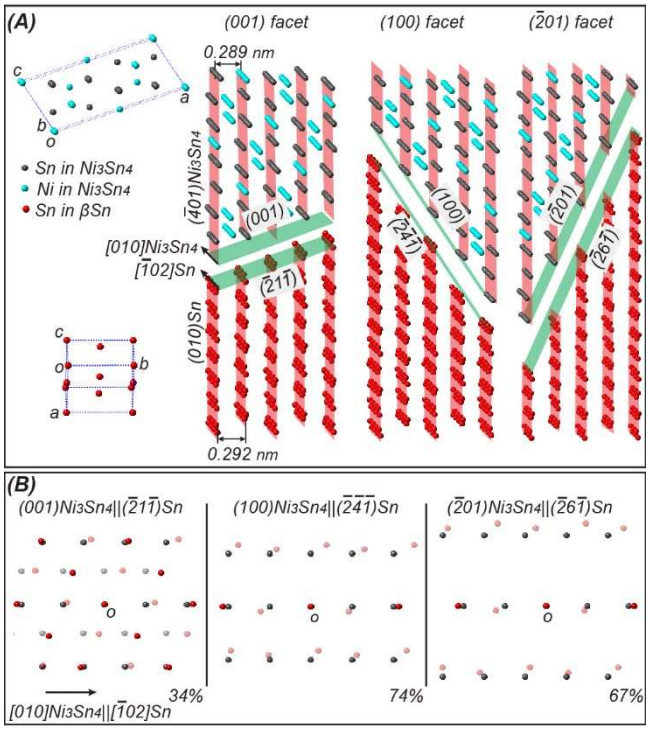

Figure 7 (A) Atomic matching between βSn and Ni_3Sn_4 on different facets. (B) Planar atomic matching of interfaces on the three facets. All near-interface atoms are projected into the plane. Transparent atoms are out of plane.

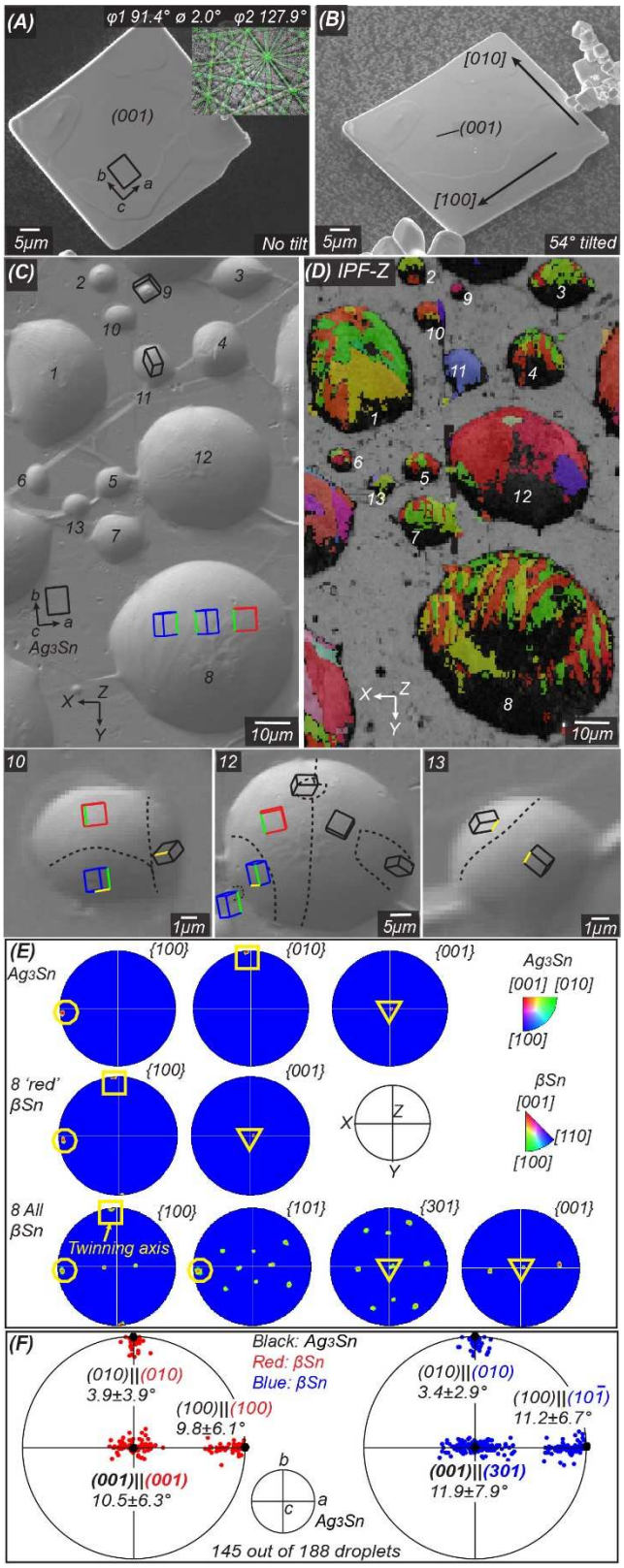

Figure 8 (A) A typical Ag_3Sn single crystal indexed as *oP8*-Ag_3Sn [42] by EBSD. (B) The same crystal that is 54° tilted to the electron beam direction. (C) Typical Sn droplets on Ag_3Sn, with βn orientations shown with unit cell wireframes. (D) EBSD IPF-Z map. (E) Pole figures of droplet 8 and the Ag_3Sn crystal. To represent the OR, parallel planes and directions in the βSn and the Ag_3Sn are indicated by the same symbols. Triangles indicate the facet of the Ag_3Sn and corresponding parallel plane in βSn. (F) Orientations of βSn grains that have the ORs in Eq. 5 and Eq. 6 with Ag_3Sn summarised into pole figures with respect to Ag_3Sn (see the reference coordinate system).

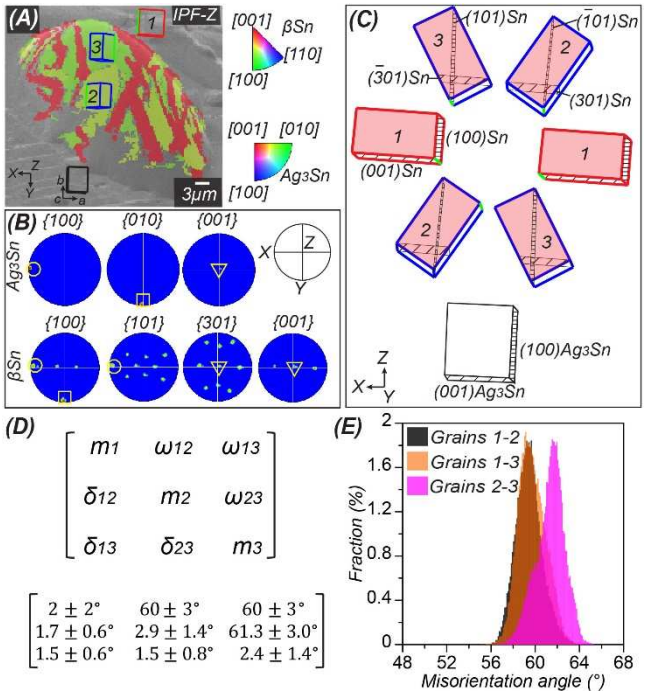

Figure 9 (A) A typical droplet on Ag_3Sn with interlaced-twinned βSn structure with an EBSD IPF-Z map and unit cell wireframes superimposed. (B) Corresponding pole figures with parallel planes and directions labelled using the same symbols. (C) The OR between cyclic twinned βSn grains and Ag_3Sn created by translating the unit cells and rotating all orientations in (A) 90° upwards (see their coordinate systems). Parallel planes in βSn and Ag_3Sn are indicated by black shaded planes. Red planes indicate the common plane of cyclic twinned βSn grains. (D) Misorientations δ_{ij} between twinning axes, in-grain misorientation m_i, and the misorientation ω_{ij} between the other <100> axes of grains. (E) Angular distributions of misorientation between grains in the interlaced twins.

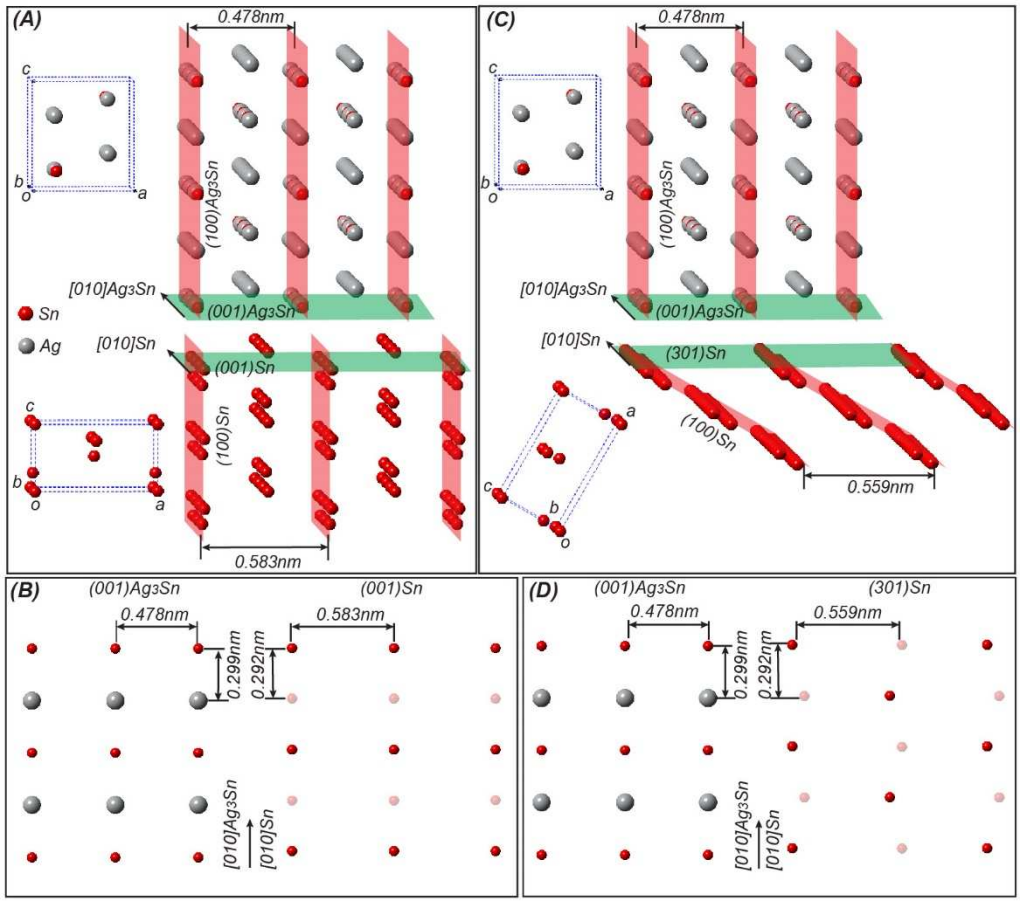

Figure 10 (A) Atomic matching between βSn and Ag_3Sn in (A) OR in Eq. 5 and (C) OR in Eq. 6. (B) and (D) The corresponding interfacial atomic match shown by projecting all near-interface atoms into the plane. Transparent atoms are out of plane.

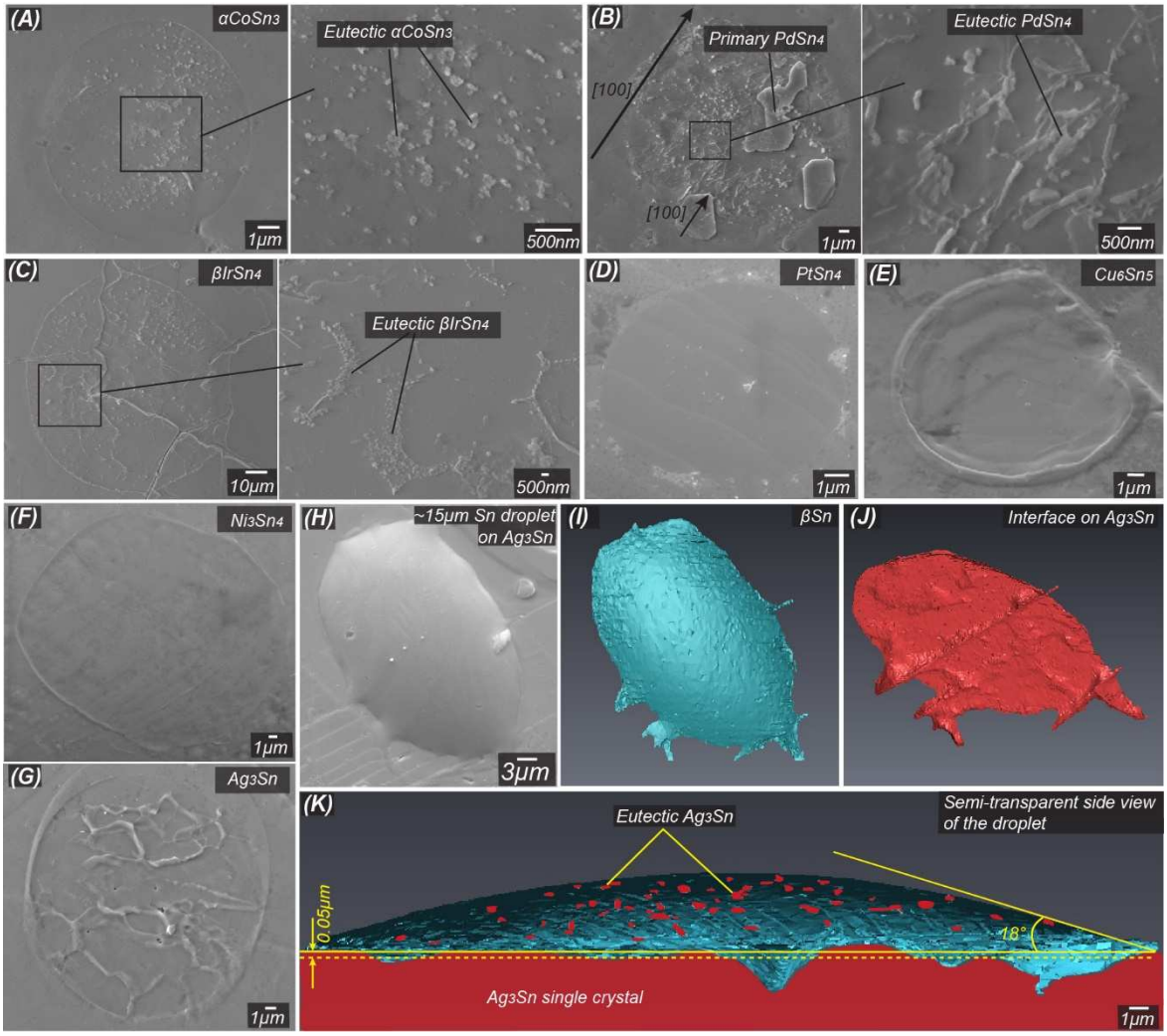

Figure 11 Interfaces of Sn droplets on IMCs after dissolving all βSn: (A) $\alpha CoSn_3$, (B) $PdSn_4$, (C) $\beta IrSn_4$, (D) $PtSn_4$, (E) Cu_6Sn_5, (F) Ni_3Sn_4, and (G) Ag_3Sn. (H)-(K) FIB-tomography of the Sn droplet on Ag_3Sn in Figure 9: (H) the secondary electron image, (I) reconstructed tin droplet, (J) the interface on Ag_3Sn, and (K) a semi-transparent side view showing the wetting angle and the average dissolved thickness of the Ag_3Sn single crystal.

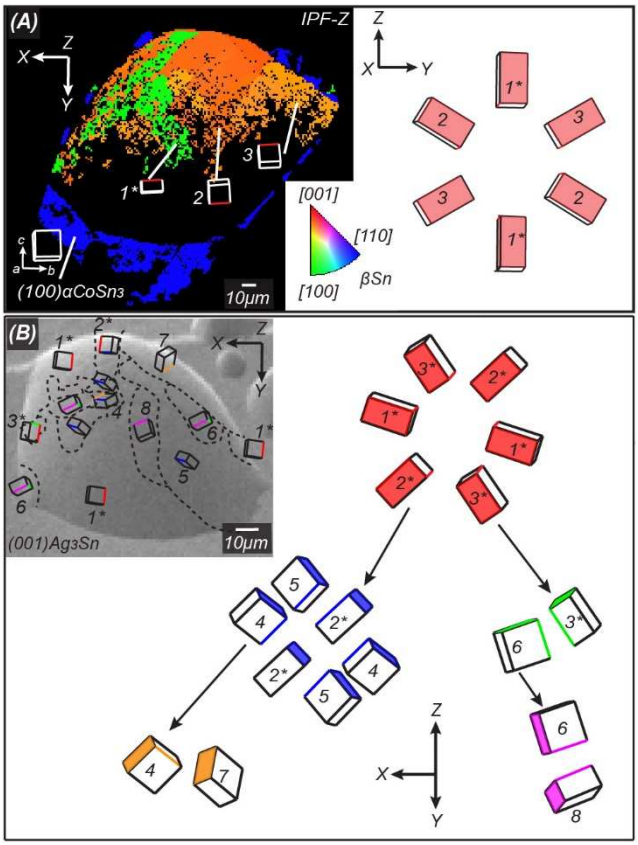

Figure 12 (A) A Sn-3.0Ag-0.5Cu droplet on a (100)αCoSn$_3$ facet and the EBSD IPF-Z map of βSn in this droplet. The orientations of the cyclic twinned βSn grains are shown in the {101} type twinning configuration. (B) A Sn droplet on a (001)Ag$_3$Sn facet showing 5 interrelated twins as indicated by the superimposed βSn unit cell wireframes and coloured twinning axes. Arrows show orientations that are shared between two rings of cyclic twins.

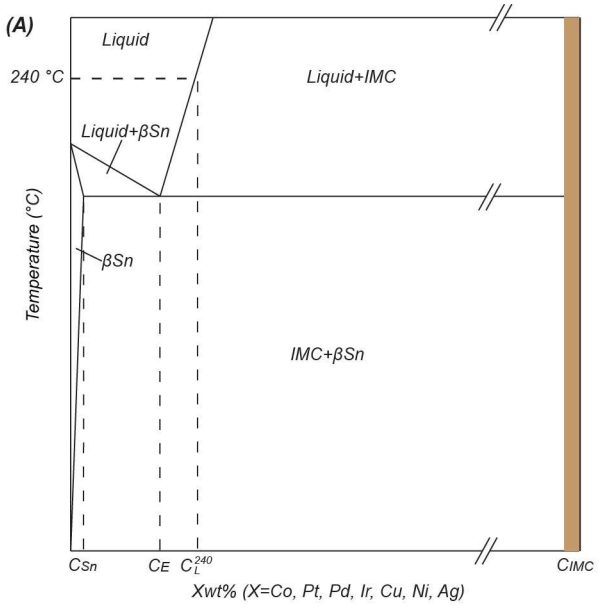

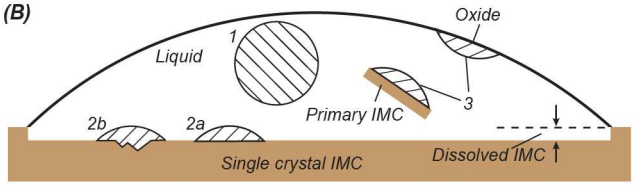

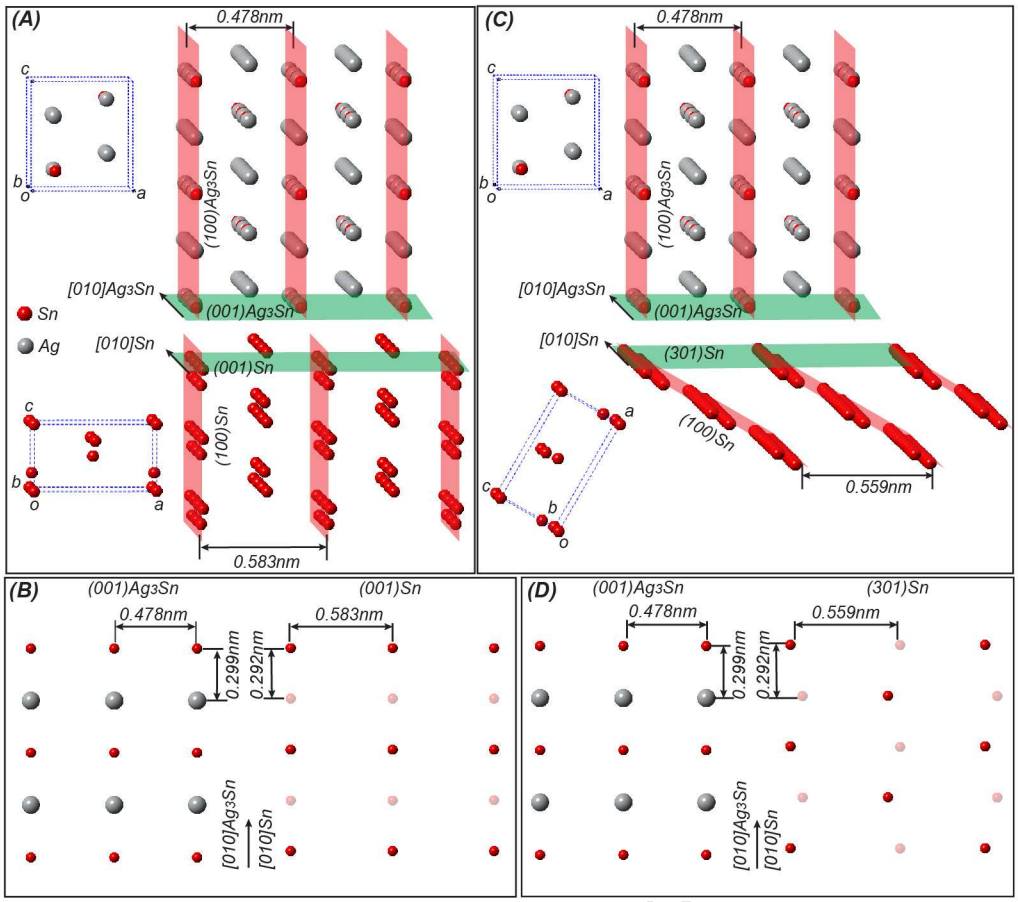

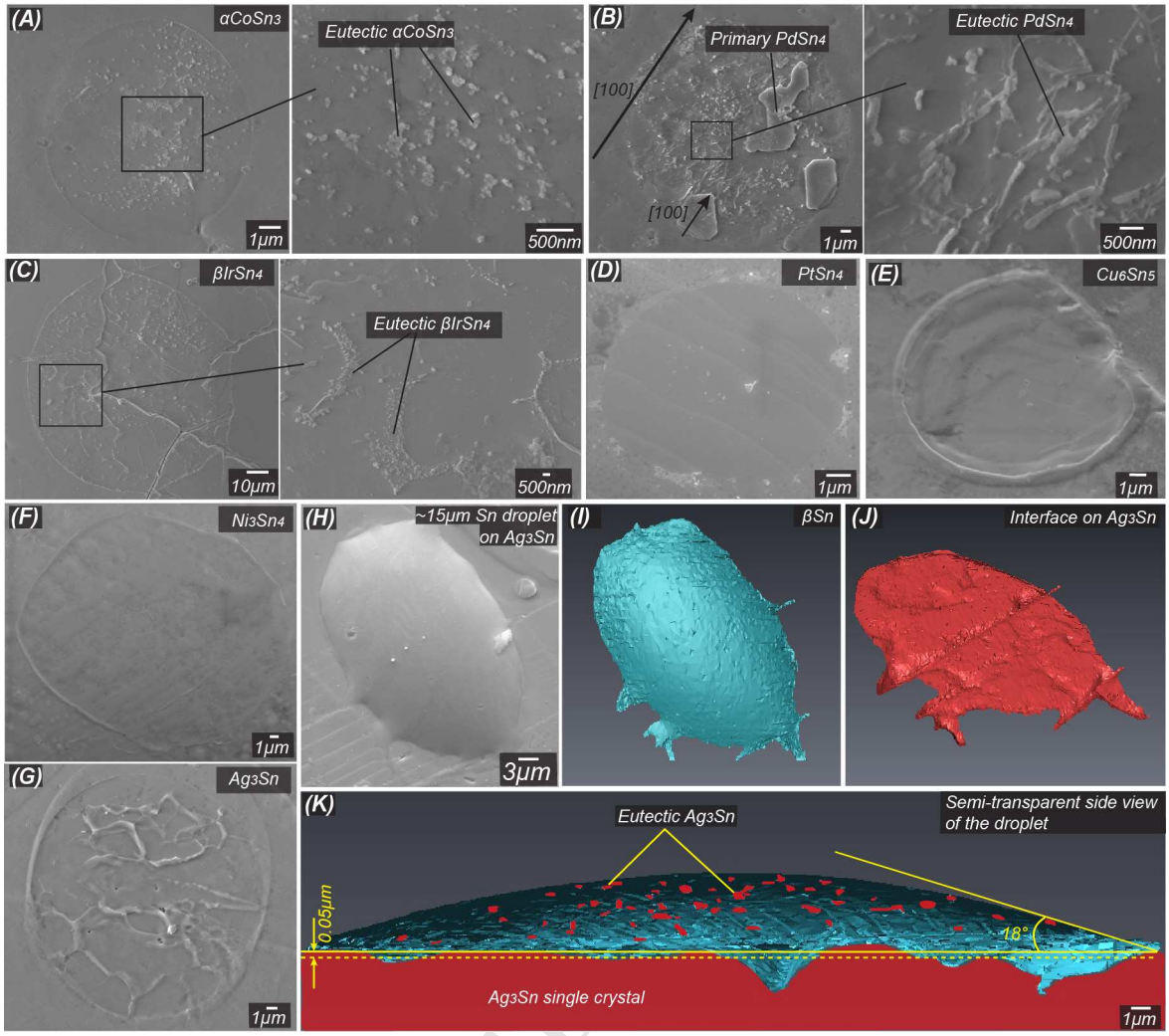

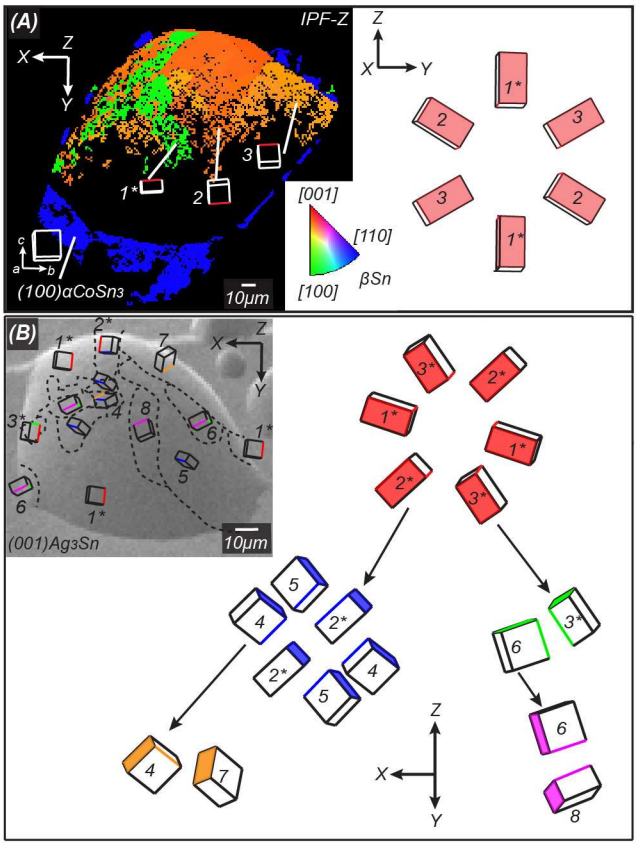

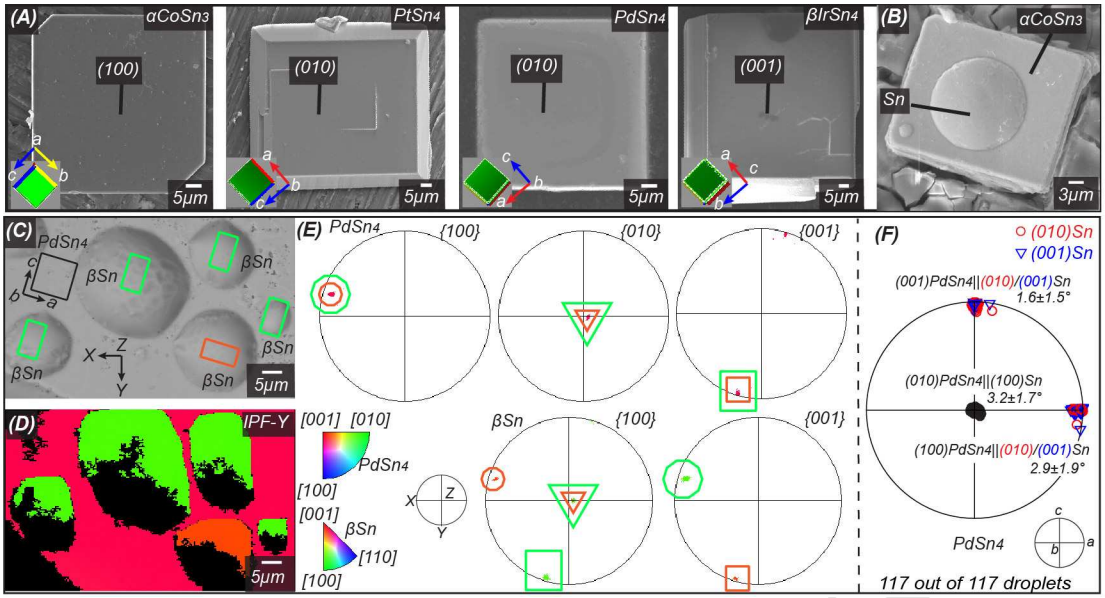

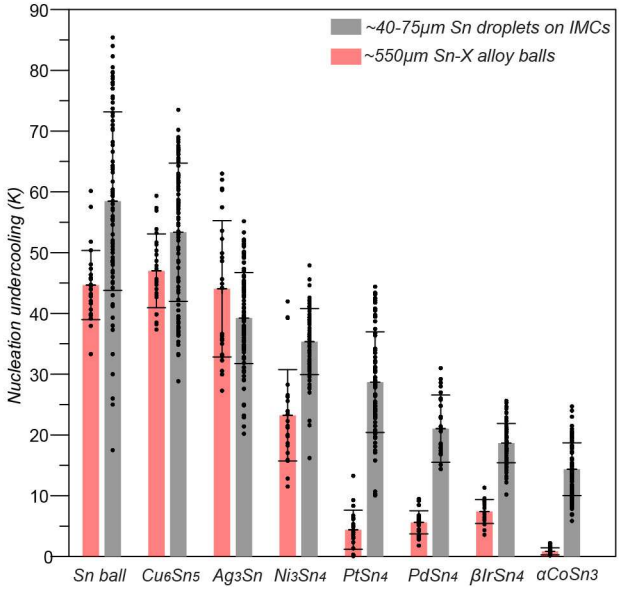

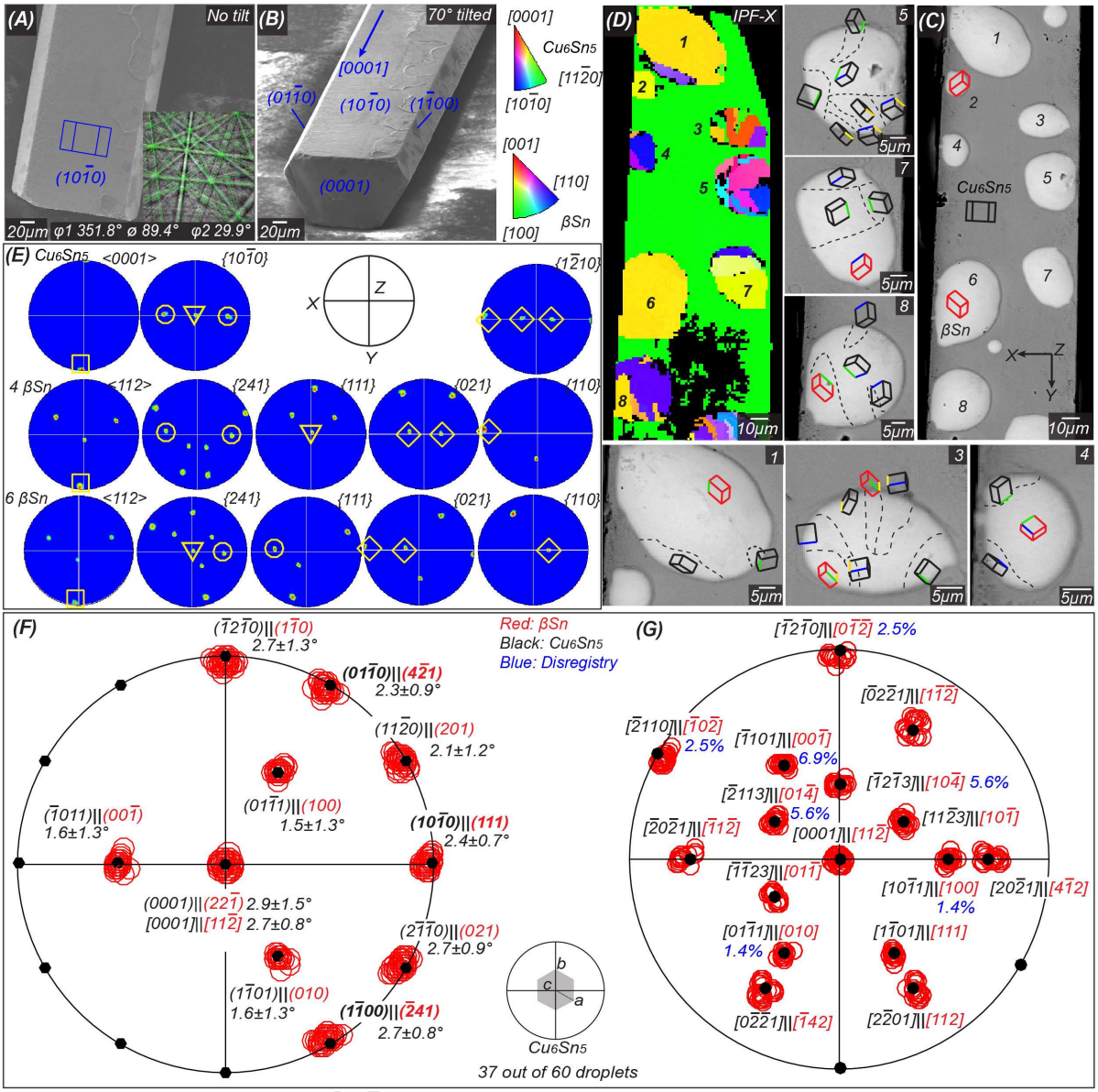
(A)
No tilt
(10$\bar{1}$0)
20μm φ1 351.8° ø 89.4° φ2 29.9°
(B)
70° tilted
[0001]
(01$\bar{1}$0)
(10$\bar{1}$0)
(1$\bar{1}$00)
(0001)
20μm
[0001]
Cu6Sn5
[11$\bar{2}$0]
[10$\bar{1}$0]
[001]
[110]
βSn
[100]
(D)
IPF-X
1
2
3
4
5
6
7
8
10μm
5μm
(C)
Cu6Sn5
βSn
X
Z
Y
(E) Cu6Sn5 <0001> {10$\bar{1}$0} {1$\bar{2}$10}
4 βSn <112> {241} {111} {021} {110}
6 βSn <112> {241} {111} {021} {110}
(F)
Red: βSn
Black: Cu6Sn5
Blue: Disregistry
(0001)||(22$\bar{1}$) 2.9±1.5°
[0001]||[11$\bar{2}$] 2.7±0.8°
(01$\bar{1}$0)||(4$\bar{2}$1) 2.3±0.9°
(11$\bar{2}$0)||(201) 2.1±1.2°
(01$\bar{1}$1)||(100) 1.5±1.3°
(10$\bar{1}$0)||(111) 2.4±0.7°
($\bar{1}$011)||(00$\bar{1}$) 1.6±1.3°
(2$\bar{1}$$\bar{1}$0)||(021) 2.7±0.9°
(1$\bar{1}$01)||(010) 1.6±1.3°
(1$\bar{1}$00)||($\bar{2}$41) 2.7±0.8°
b
c
a
Cu6Sn5
37 out of 60 droplets
(G)
[$\bar{1}$2$\bar{1}$0]||[0$\bar{1}$$\bar{2}$] 2.5%
[$\bar{2}$110]||[$\bar{1}$0$\bar{2}$] 2.5%
[$\bar{1}$101]||[00$\bar{1}$] 6.9%
[0$\bar{2}$$\bar{2}$1]||[1$\bar{1}$$\bar{2}$]
[$\bar{2}$113]||[01$\bar{4}$] 5.6%
[$\bar{1}$2$\bar{1}$3]||[10$\bar{4}$] 5.6%
[$\bar{2}$0$\bar{2}$1]||[$\bar{1}$1$\bar{2}$]
[0001]||[11$\bar{2}$]
[11$\bar{2}$3]||[10$\bar{1}$]
[$\bar{1}$$\bar{1}$23]||[01$\bar{1}$]
[10$\bar{1}$1]||[100] 1.4%
[20$\bar{2}$1]||[4$\bar{1}$2]
[01$\bar{1}$1]||[010] 1.4%
[1$\bar{1}$01]||[111]
[0$\bar{2}$$\bar{2}$1]||[$\bar{1}$42]
[2$\bar{2}$01]||[112]

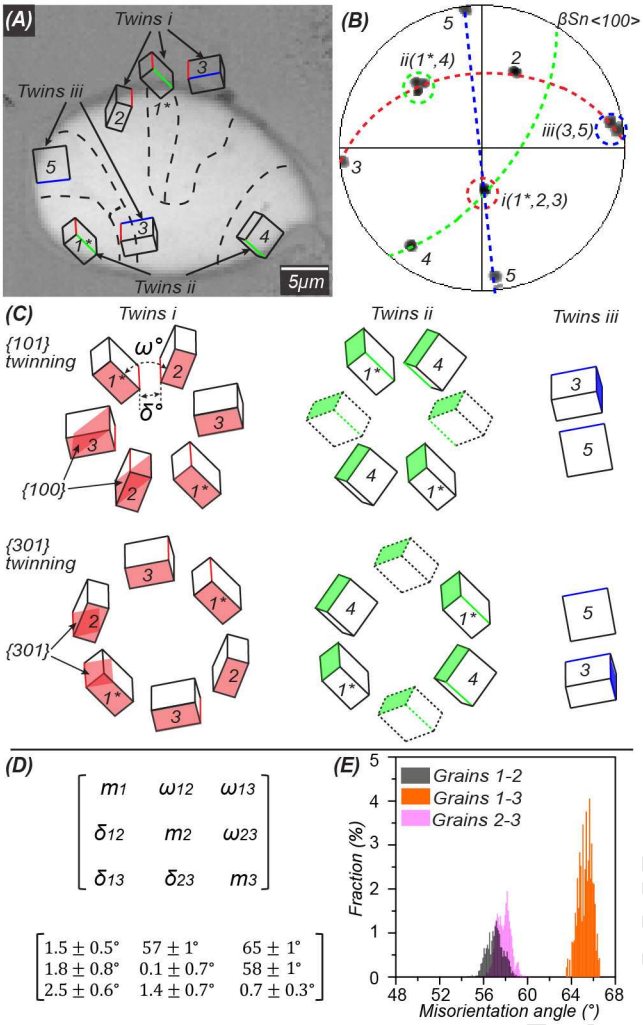

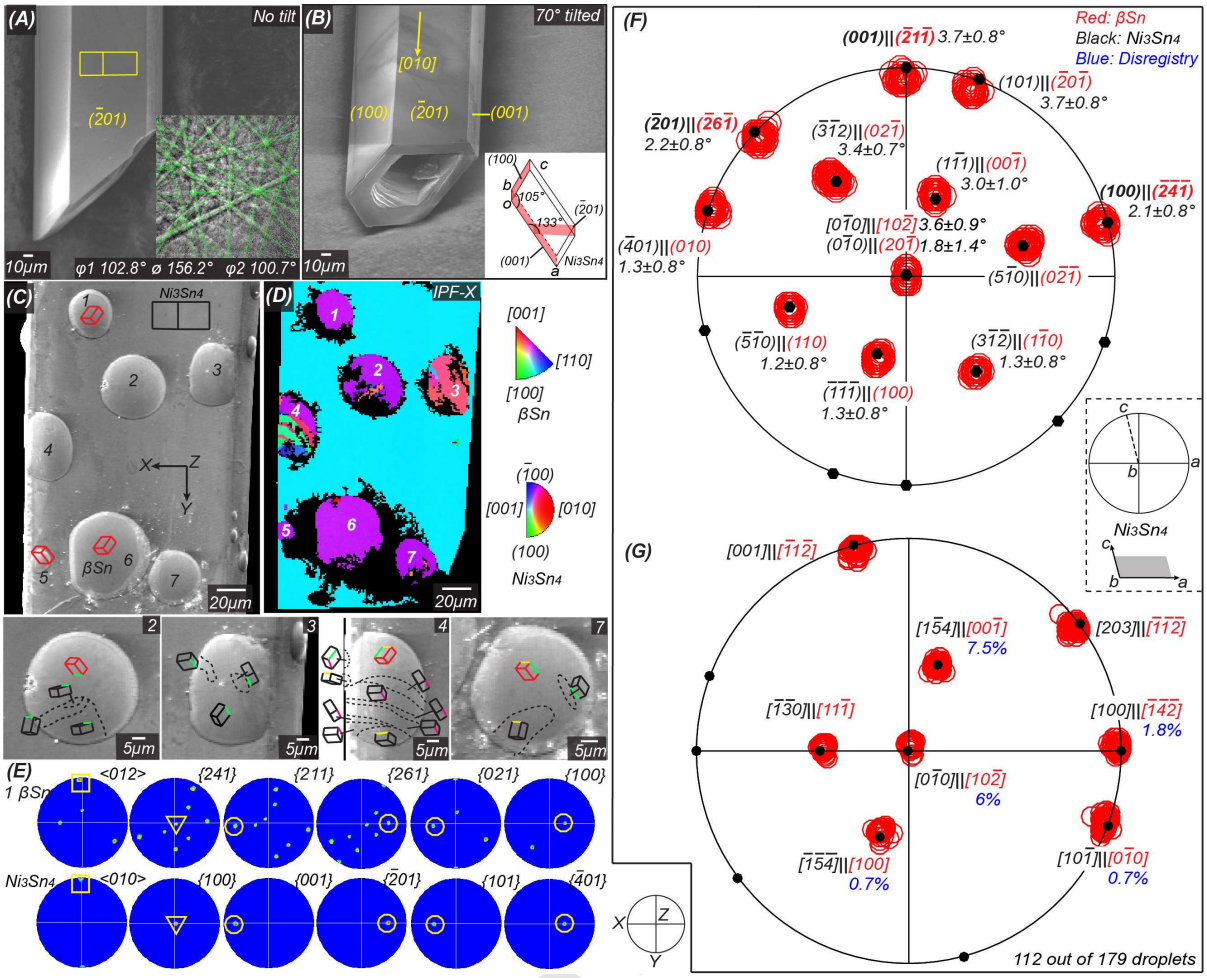
(A)
No tilt
(B)
70° tilted
(C)
(D)
IPF-X
(E)
(F)
Red: βSn
Black: Ni3Sn4
Blue: Disregistry
(G)
112 out of 179 droplets

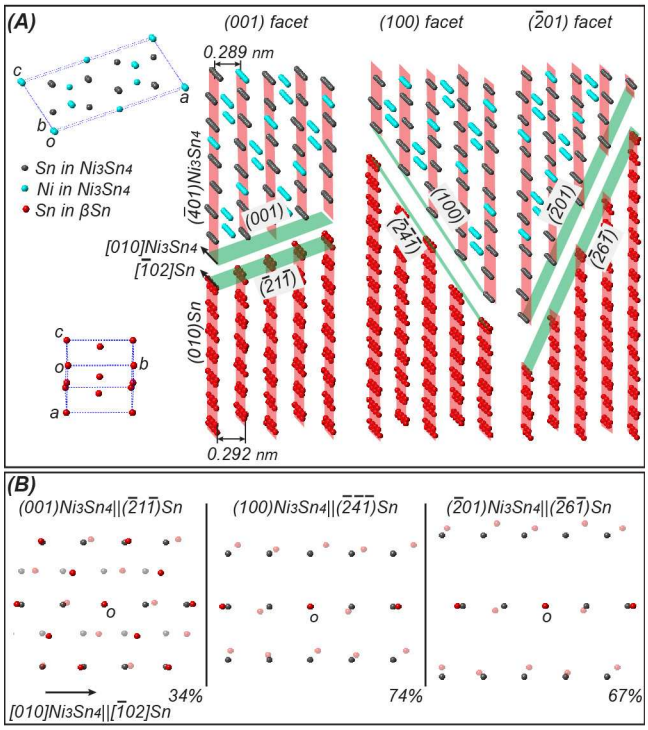

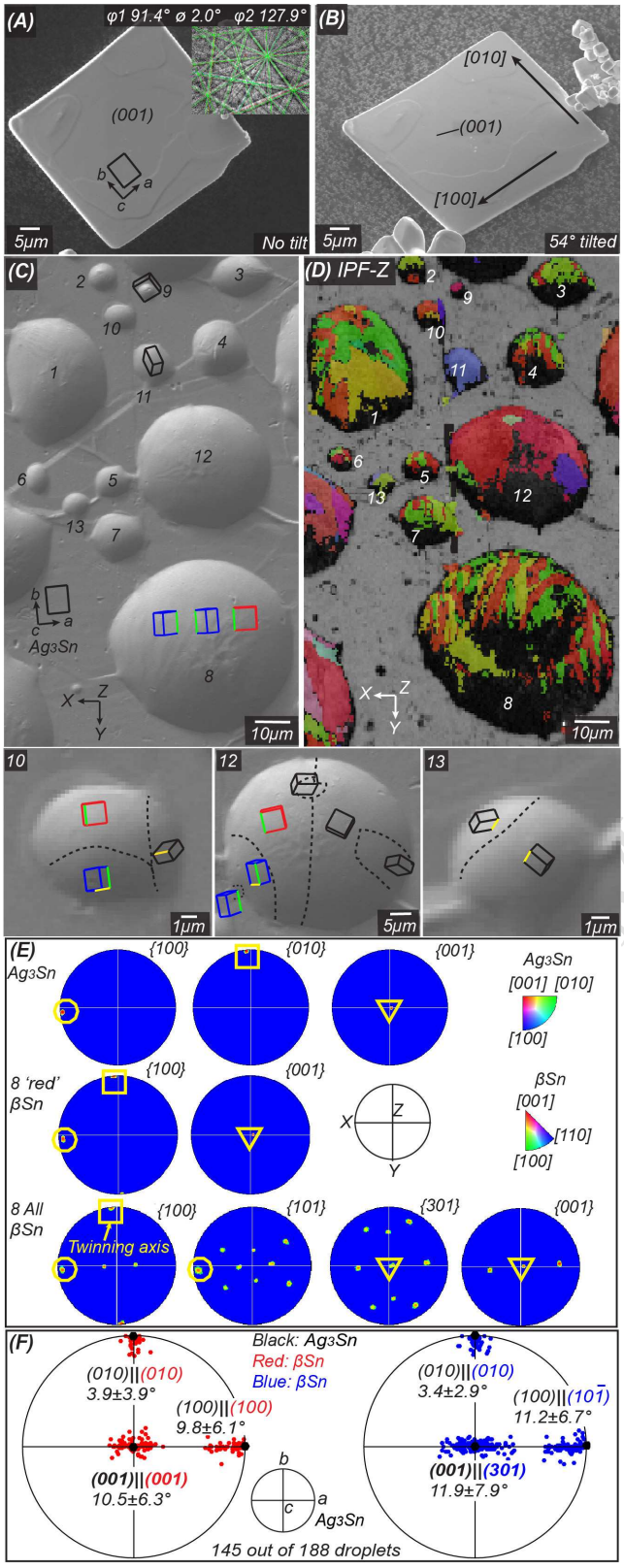
(A)
φ1 91.4° ø 2.0° φ2 127.9°
(001)
b
a
c
5μm
No tilt
(B)
[010]
(001)
[100]
5μm
54° tilted
(C)
Ag3Sn
10μm
(D) IPF-Z
10μm
10
1μm
12
5μm
13
1μm
(E)
Ag3Sn
{100}
{010}
{001}
[001] [010]
[100]
8 'red' βSn
βSn
[001]
[110]
8 All βSn
Twinning axis
{101}
{301}
(F)
Black: Ag3Sn
Red: βSn
Blue: βSn
(010)||(010)
3.9±3.9°
(100)||(100)
9.8±6.1°
(001)||(001)
10.5±6.3°
3.4±2.9°
(100)||(10$\bar{1}$)
11.2±6.7°
(001)||(301)
11.9±7.9°
145 out of 188 droplets

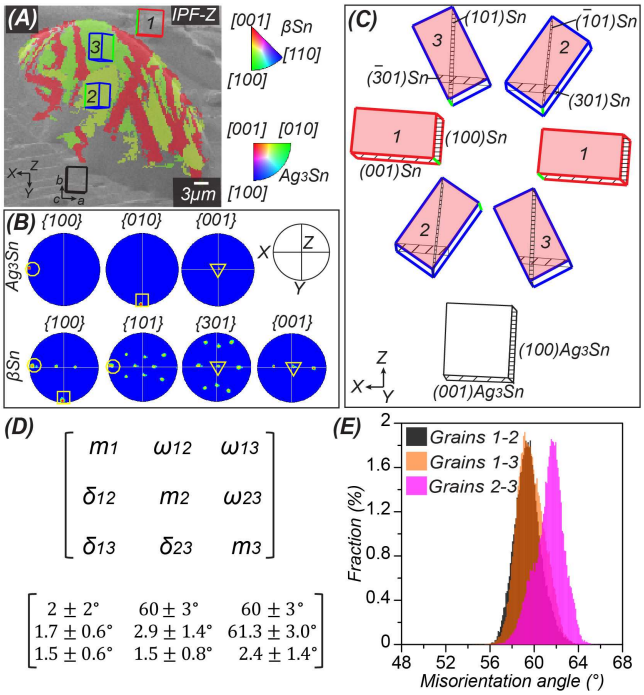

(D)

$$\begin{bmatrix} m_1 & \omega_{12} & \omega_{13} \\ \delta_{12} & m_2 & \omega_{23} \\ \delta_{13} & \delta_{23} & m_3 \end{bmatrix}$$

$$\begin{bmatrix} 2 \pm 2^\circ & 60 \pm 3^\circ & 60 \pm 3^\circ \\ 1.7 \pm 0.6^\circ & 2.9 \pm 1.4^\circ & 61.3 \pm 3.0^\circ \\ 1.5 \pm 0.6^\circ & 1.5 \pm 0.8^\circ & 2.4 \pm 1.4^\circ \end{bmatrix}$$